Title
Single Cell Molecular and Biophysical Phenotyping

Author
Lin, Jonathan

Publication Date
2018

Peer reviewed|Thesis/dissertation

UNIVERSITY OF CALIFORNIA

Los Angeles

Single Cell Molecular and Biophysical Phenotyping

A dissertation submitted in partial satisfaction

of the requirements for the degree

Doctor of Philosophy in Bioengineering

by

Jonathan Lin

2018

ABSTRACT OF THE DISSERTATION

Single Cell Molecular and Biophysical Phenotyping

by

Jonathan Lin
Doctor of Philosophy in Bioengineering
University of California, Los Angeles, 2018
Professor Dino Di Carlo, Chair

Understanding cellular heterogeneity is a crucial part of modern biomedical research as well as medical diagnostics and therapeutics. A multitude of technologies have emerged to perform single cell measurements, but low throughput and high cost remain barriers to largescale adoption. This dissertation discusses the development of three single cell techniques that enable new measurement modalities in addition to improving throughput. Two of the described technologies are label-free assays, measurements that do not require molecular labels and as a result, are cheaper, faster, and less invasive ways of measuring cell state.

Chapter 1 discusses the importance of single cell measurements and the benefits of label-free assays. Chapter 2 discusses Multiparameter Deformability Cytometry, a label-free technique to measure the physical properties of cells. This technique builds upon previous deformability cytometry work by extending measurement capabilities to include cellular morphology and deformation kinetics. We demonstrate the usefulness of the new system by measuring and classifying stem cells and their descendants based on mechanical phenotype alone. Chapter 3 discusses the development of a parallel flow cytometer. By integrating an ultrafast fluorescence imaging technology with a novel microfluidic flow cell, we are able to increase sample throughput by interrogating up to eight samples simultaneously. Chapter 4 describes a technology that bridges the gap between conventional biomolecular measurements and physical phenotype measurements. By once again integrating an ultrafast imaging

technique with a novel microfluidic flow cell, we can perform simultaneous biochemical and physical measurements on single cells. Additionally, by staining subcellular structures, we can begin to investigate the mechanical properties of cellular components such as the nucleus. We demonstrate the capabilities of the system by measuring the deformability of cells after treatment with various cytoskeletal agents as well as by osmotically shocking cells and observing changes to their nuclear and cytoplasmic deformations.

The dissertation of Jonathan Lin is approved.

Pei Yu Chiou

Amy Catherine Rowat

Michael Alan Teitell

Dino Di Carlo, Committee Chair

University of California, Los Angeles

2018

To my wife, my family, and my dog.

TABLE OF CONTENTS

LIST OF FIGURES

LIST OF TABLES

ACKNOWLEDGMENTS

Chapter 2 is adapted from "High-throughput physical phenotyping of cell differentiation". Microsystems and Nanoengineering 3, 17013 (2017). JL and DK designed and conducted experiments and prepared the manuscript. PT, LP, MD, and SK assisted with experiments. HT assisted with automated analysis code. DD provided guidance for experiments and manuscript preparation.

Chapter 3 contains sections from a work in preparation by Lin *et al.* entitled "A High-throughput, inertial-microfluidic, digital, radiofrequency-encoded array (HIDRA) parallel flow cytometer."

Chapter 4 contains sections from a work in preparation by Lin J, Munoz H, *et al.* entitled "Integrated deformability and fluorescence imaging cytometry."

Additional acknowledgments:

This thesis would not have been possible without the support of my family, my friends and my colleagues. I am endlessly thankful for all of the help, advice, and encouragement they have given me over the years.

I would like to thank my advisor, Dino Di Carlo, for giving me the opportunity to explore wherever my curiosity led me and for his dedication to training good people, not just good scientists and engineers. He was equally adept as an advisor, a role model, and someone to geek out over a paper with. I was incredibly fortunate to find a mentor with the patience to let me learn from my (many) mistakes.

I would also like to thank all the members of the Di Carlo lab. Thanks for humoring my half-baked ideas and putting up with my antics. In particular, I would like to thank Manjima Dhar and Ivan Pushkarsky who were always there for me to bounce ideas off of and who were always willing to commiserate over a drink at Barney's.

I would especially like to thank my family - my brother, Clifford, for being endlessly supportive and for reminding me to stay humble and grounded. My parents, who taught

me to persevere and to always set my sights high. None of this would have been possible without them.

Finally, I would like to thank my wife, Christine Wang, for her unwavering love, her steadfast support, and her uncanny ability to knock me off my high horse. I look forward to our future adventures and achievements. I also could not ask for a better collaborator in life.

VITA

2007–2011	B.S. in Biomedical Engineering, Northwestern University
2011–present	M.D. student, University of California, Los Angeles
2013–present	Ph.D. student in Bioengineering, University of California, Los Angeles

PUBLICATIONS

Peter Tseng, **Jonathan Lin**, Keegan Owsley, Janay Kong, Anja Kunze, Coleman Murray, and Dino Di Carlo. "Flexible and Stretchable Micromagnet Arrays for Tunable Biointerfacing". In: *Advanced Materials.* 27.6 (2015), pp: 1083-1089

Anja Kunze, Coleman Murray, Chanya Godzich, **Jonathan Lin**, Keegan Owsley, Andy Tay, and Dino Di Carlo. "Modulating motility of intracellular vesicles in cortical neurons with nanomagnetic forces on-chip". In: *Lab on a Chip.* 17.5 (2017), pp: 842-854

Jonathan Lin, Donghyuk Kim, Henry T. Tse, Peter Tseng, Lillian Peng, Manjima Dhar, Saravanan Karumbayaram, and Dino Di Carlo. "High-throughput physical phenotyping of cell differentiation". In: *Microsystems and Nanoengineering.* 3 (2017), 17013

Christine E. Wang, Roma C. Yumul, **Jonathan Lin**, Yilong Cheng, Andre Lieber, Suzie H. Pun. "Junction opener protein increases nanoparticle accumulation in solid tumors". In: *Journal of Controlled Release.* 272.28 (2018), pp: 9-16

Ivan Pushkarsky, Peter Tseng, Dylan Black, Bryan France, Lyndon Warfe, Cynthia J. Koziol-

White, William F. Jester Jr, Ryan K. Trinh, **Jonathan Lin**, Philip O. Scumpia, Sherie L. Morrison, Reynold A. Panettieri Jr, Robert Damoiseaux and Dino Di Carlo. "Elastomeric sensor surfaces for high-throughput single-cell force cytometry". In: *Nature Biomedical Engineering.* 2 (2018), pp: 124-137

Hector E. Munoz, Ming Li, Carson T. Riche, Nao Nitta, Eric Diebold, **Jonathan Lin**, Keegan Owsley, Matthew Bahr, Keisuke Goda, and Dino Di Carlo. "Single-Cell Analysis of Morphological and Metabolic Heterogeneity in *Euglena gracilis* by Fluorescence-Imaging Flow Cytometry". In: *Analytical Chemistry. In Press.*

CHAPTER 1

Introduction

The measurement of cellular properties has long been core to our modern understanding of biology and human physiology. In recent years, advances in medical technology including immunotherapy and personalized medicine have been enabled by cytometry but have also revealed a growing need for new cytometry technologies. One major trend in cytometry is a focus on single-cell measurements that enable researchers and physicians to detect and understand the heterogeneity present within populations of cells. Related to this, there is a trend towards technologies with higher throughputs that boast increased statistical power when studying rare cells and enable cytometry to scale up towards the throughputs needed in personalized medicine and drug discovery. Another field of growing interest is label-free assays, cellular measurements that do not require molecular labels such as antibodies. In this chapter, we will discuss each of these trends in turn and in subsequent chapters we will present three technologies that we have developed to help overcome these technological hurdles.

1.1 Single-cell Cytometry

The ability to detect and characterize cellular heterogeneity is essential to a nuanced understanding of biology. The ability to detect subpopulations of cells has proven to be invaluable in a wide variety of biomedical applications.

In the detection and study of disease, for instance, subpopulations of cells can be responsible for the majority of disease burden or can rapidly become the dominant phenotype if ignored. Recent research has focused on heterogeneity in tumors as a reservoir of diversity

that can give rise to treatment resistance. As a result, there is an increased focus on measuring diversity through techniques such as spatial and temporal sampling and technologies such as single-cell sequencing.[1] Similarly, recent research has revealed that, in addition to genetic mutations, diversity in the expression and activity of critical bacterial cell processes can give rise to antibiotic resistance.[2] Rare cells can even dictate the prognosis of disease. Circulating tumor cells, because they can give rise to lethal metastatic tumors, can be the dominant influence on disease burden and patient outcomes while existing as an overwhelming minority of neoplastic cells by count.[3–5]

Cellular diversity is also important in the development of therapeutics. This is especially true in light of the development and commercialization of chimeric antigen receptor (CAR) T cells as a cancer treatment. In all cell-based therapies, the ability to detect and enrich cells of a specific phenotype, whether that is expression of a chimeric antigen receptor or the ability to infiltrate and survive within tumors, is crucial.[6,7] The importance of heterogeneity will only become more pronounced as CAR-T cells are brought to bear against solid tumors where the lack of a universal marker such as CD19 will require careful antigen characterization and selection.[8]

These advances in diagnostics, therapeutics, and personalized medicine were made possible by single-cell measurement technologies. Technologies such as flow cytometry and fluorescence-activated cell sorting (FACS) have been commercially available for decades and are workhorses of both research and medicine. However, as the needs of biomedical research have evolved, cytometry technologies have evolved as well. Techniques that have traditionally been limited to aggregate measurements of large numbers of cells are being rapidly adapted to single cell formats. For instance, techniques such as single-cell nucleic acid sequencing are rapidly evolving and are available commercially.[9,10] Similarly, single-cell Western blotting is actively being developed and commercialized.[11,12] Additionally, new technologies are emerging to measure new properties of cells such as force generation and adhesion profile.[13,14] Even long-standing single cell technologies such as flow cytometry are currently being researched with many groups focusing on microfluidics as a way to improve throughput and lower cost

and on imaging as a way to increase the measurable parameter space.[15–19]

It is clear that single-cell cytometry remains a field of active interest due not only to the wide array of applications that remain to be explored but also the rapidly growing needs of the healthcare and biomedical research industries.

1.2 High-throughput Cytometry

Another active area of cytometry research is high-throughput cytometry. One of the major barriers to widespread adoption of single-cell measurement techniques is their relatively low throughput. Although commercially available flow cytometers already boast measurement rates >10,000 events/second and sample throughputs of >100 μl/minute, these throughputs remain too low for applications such as drug discovery where cell numbers in excess of a million are routinely processed. These fields continue to largely use aggregate-readout techniques such as microplate absorbance measurements, with limited use of single-cell techniques such as flow cytometry and microscopy-based high-content screening.[20–22]

As previously discussed, however, there is much to be gained by capturing cellular heterogeneity by adopting single-cell measurement techniques. These measurements are more information-rich, capable of performing multiplexed measurements at the single cell level, allowing researchers to simultaneously probe numerous properties of individual cells. For instance, flow cytometry has enabled single cell investigation of numerous drug screening-relevant experiments including antibody screening, efflux transporter activity, receptor binding, G-protein-coupled receptor activity, and in vitro toxicology.[23]

Numerous attempts have been made to improve the throughput of single-cell techniques. In the field of flow cytometry, the main approach has been to run smaller sample volumes, which reduces statistical power and imposes constraints on experimental design in order to improve sample throughput.[23] Another method has been to run multiple flow cytometers in parallel, an approach that comes at a significant monetary and complexity cost. Comparing data from multiple instruments is particularly difficult.[24,25]

New microfluidic technologies have attempted to improve cytometry throughput with a variety of approaches. Some technologies improve particle focusing through techniques such as inertial or acoustic focusing, enabling faster flow rates.[26–29] Other technologies generate multiple streams of particles, allowing higher sample throughput or simultaneous measurement of multiple samples through parallelization.[30–33] While the particle focusing approaches can yield modest improvements to sample throughput, the parallel stream approaches represent potential improvements of an order of magnitude or greater. However, these systems make significant sacrifices in their optical systems due to the difficulty of illuminating multiple spatial locations and efficiently collecting fluorescent emissions across a large field of view. Previous works have explored using scanning laser illumination systems and cameras to overcome these barriers.[31] However, these approaches lack the speed and sensitivity of photomultiplier tube (PMT) based systems. Other works have incoporated on-chip optical elements, adding complexity and cost to manufacturing.[33]

An instrument capable of bringing single-cell measurements to high-volume fields such as drug discovery has yet to emerge. Nascent techniques that parallelize measurements are promising but have yet to mature into fully integrated systems.

1.3 Label-free Cytometry

A growing area of interest in cytometry research is the use of label-free measurements, measurements that do not require the addition of molecular labels such as antibodies. These measurements can be performed a variety of ways including measuring the light scattering and attenuating properties of cells in order to assay cell cycle, cellular DNA content, and cell senescence.[34,35] Similarly, impedance measurements have been used to measure cell electrical properties, and microfluidic resonators have been used to measure cell mass and size.[36,37] Still other technologies have used soft substrates to measure the forces generated by cells.[13,38]

One set of cellular properties that is of particular interest consists of physical properties including the shape, size, and resistance of cells to an applied load. These properties are

interesting because they stem from structural and molecular cell properties in a complex fashion that is not easily discerned.[39–43] Whereas conventional molecular biomarkers indicate the presence of specific biomolecules, these physical properties integrate many molecular changes, allowing them to serve as summary measurements of cell state. Recent findings demonstrate that physical properties are a promising alternative for phenotyping a range of cell types in different stages. For instance, recent studies have revealed that the differentiation potential of mesenchymal stromal/stem cells is strongly dependent upon their elastic and viscoelastic properties and that mechanical markers can help predict osteogenesis in differentiating stem cells.[44,45] Other work has demonstrated that physical changes contribute to natural phenomena such as leukocyte demargination.[46]

Although physical properties are promising biomarkers of cell state, performing quantitative and reliable physical measurements for large population of cells has always been challenging.[47] Conventional approaches, such as atomic force microscopy (AFM) or micropipette aspiration (MA), provide reliable measurements of the effective Young's modulus of individual cells.[48,49] Unfortunately, these methods are both labor intensive and time consuming (tens of cells per hour), making it difficult to achieve statistical power or detect rare cell populations. Recent advances in micro-/nano-fabrication technologies, however, have enabled new mechanophenotyping technologies that can measure deformations of tens to hundreds of cells per second.[50–58]

Recent work in our lab on a technique called deformability cytometry has enabled single-cell mechanophenotyping at 2,000 cells per second. This system integrates an inertial microfluidic chip and a high-speed camera in order to measure cell size and deformation upon exposure to uniform hydrodynamic stress.[59] Deformability cytometry's ability to assay cell state was demonstrated by successfully discriminating activated/non-activated leukocytes and identifying malignancy in pleural effusion samples.[60]

Physical properties hold great promise as biomarkers for cell state and may be useful in the detection of disease. However, physical properties remain relatively unexplored. Further research is needed to identify and characterize new, useful physical properties. Additionally,

mechanophenotyping systems need to be integrated with traditional cytometry techniques so that the strengths of both approaches can be combined.

1.4 New Approaches to High-throughput, Single-cell cytometry

In the following three chapters, we describe three cytometry technologies that we have developed to address the need for high-throughput, single-cell measurement techniques.

The first technology, Multiparameter Deformability Cytometry, is a high-throughput, label-free technique to measure the physical properties of single cells. This technique extends previous work on deformability cytometry, adding the ability to measure cellular morphology and deformation kinetics. The usefulness of the technique is demonstrated by measuring and classifying stem cells and their descendants based on mechanical phenotype.

The second technology is a parallel flow cytometer. The system integrates an ultrafast fluorescence imaging technology with a novel microfluidic flow cell, enabling a dramatic increase in sample throughput by interrogating up to eight samples simultaneously. This technology is targeted towards drug discovery and personalized medicine applications where high sample throughput, in addition to high event rates, is a key requirement.

The third technology is one that combines conventional biomolecular measurements and physical phenotype measurements. Through integration of an ultrafast imaging technique with a novel microfluidic flow cell, we perform simultaneous biochemical and physical measurements on single cells. The imaging capabilities of the system can further be used to investigate the mechanical properties of subcellular components such as the nucleus. This technology enables the study of the molecular underpinnings of cell mechanical properties and the mechanical phenotypes of different cellular subpopulations.

1.5 References

[1] Ibiayi Dagogo-Jack and Alice T. Shaw. *Tumour heterogeneity and resistance to cancer therapies*. Nov. 2018.

[2] M. A. Sanchez-Romero and J. Casadesus. "Contribution of phenotypic heterogeneity to adaptive antibiotic resistance". In: *Proceedings of the National Academy of Sciences* 111.1 (2014), pp. 355–360.

[3] Matthew G Krebs et al. "Evaluation and prognostic significance of circulating tumor cells in patients with non-small-cell lung cancer". In: *Journal of Clinical Oncology* 29.12 (Apr. 2011), pp. 1556–1563.

[4] Massimo Cristofanilli et al. "Circulating Tumor Cells, Disease Progression, and Survival in Metastatic Breast Cancer". In: *New England Journal of Medicine* 351.8 (Aug. 2004), pp. 781–791.

[5] Angela Alama et al. *Prognostic and predictive relevance of circulating tumor cells in patients with non-small-cell lung cancer*. Oct. 2014.

[6] Steven A Rosenberg and Nicholas P Restifo. *Adoptive cell transfer as personalized immunotherapy for human cancer*. Apr. 2015.

[7] Carl H June et al. "CAR T cell immunotherapy for human cancer." In: *Science (New York, N.Y.)* 359.6382 (Mar. 2018), pp. 1361–1365.

[8] Maria Michela D'Aloia et al. "CAR-T cells: the long and winding road to solid tumors". In: *Cell Death & Disease* 9.3 (Mar. 2018), p. 282.

[9] Charles Gawad, Winston Koh, and Stephen R. Quake. "Single-cell genome sequencing: current state of the science". In: *Nature Reviews Genetics* 17.3 (Mar. 2016), pp. 175–188.

[10] S. Steven Potter. "Single-cell RNA sequencing for the study of development, physiology and disease". In: *Nature Reviews Nephrology* 14.8 (Aug. 2018), pp. 479–492.

[11] Alex J Hughes et al. “Single-cell western blotting”. In: *Nature Methods* 11.7 (July 2014), pp. 749–755.

[12] Chi-Chih Kang et al. “Single cell–resolution western blotting”. In: *Nature Protocols* 11.8 (July 2016), pp. 1508–1530.

[13] Ivan Pushkarsky et al. “Elastomeric sensor surfaces for high-throughput single-cell force cytometry”. In: *Nature Biomedical Engineering* 2.2 (Feb. 2018), pp. 124–137.

[14] Harsha Kittur et al. “Probing Cell Adhesion Profiles with a Microscale Adhesive Choice Assay”. In: *Biophysical Journal* 113.8 (Oct. 2017), pp. 1858–1867.

[15] Hamed Amini, Wonhee Lee, and Dino Di Carlo. “Inertial microfluidic physics”. In: *Lab on a Chip* 14.15 (July 2014), p. 2739.

[16] C. Wyatt Shields et al. “Translating microfluidics: Cell separation technologies and their barriers to commercialization”. In: *Cytometry Part B: Clinical Cytometry* 92.2 (Mar. 2017), pp. 115–125.

[17] Eric D. Diebold et al. “Digitally synthesized beat frequency multiplexing for sub-millisecond fluorescence microscopy”. In: *Nature Photonics* 7.10 (2013), pp. 806–810.

[18] Sadao Ota et al. “Ghost cytometry.” In: *Science (New York, N.Y.)* 360.6394 (June 2018), pp. 1246–1251.

[19] Nao Nitta et al. “Intelligent Image-Activated Cell Sorting.” In: *Cell* 0.0 (Aug. 2018).

[20] J P Hughes et al. “Principles of early drug discovery.” In: *British journal of pharmacology* 162.6 (Mar. 2011), pp. 1239–49.

[21] Michael Boutros, Florian Heigwer, and Christina Laufer. “Microscopy-Based High-Content Screening”. In: *Cell* 163.6 (Dec. 2015), pp. 1314–1325.

[22] Bruce S. Edwards and Larry A. Sklar. *Flow cytometry: Impact on early drug discovery.* July 2015.

[23] Christopher B. Black et al. “Cell-Based Screening Using High-Throughput Flow Cytometry”. In: *ASSAY and Drug Development Technologies* 9.1 (2011), pp. 13–20.

[24] Robert A. Hoffman and James C.S. Wood. "Characterization of Flow Cytometer Instrument Sensitivity". In: *Current Protocols in Cytometry*. Vol. Chapter 1. Hoboken, NJ, USA: John Wiley & Sons, Inc., Apr. 2007, Unit1.20.

[25] David R. Parks et al. "Evaluating flow cytometer performance with weighted quadratic least squares analysis of LED and multi-level bead data". In: *Cytometry Part A* 91.3 (2017), pp. 232–249.

[26] Aram J. Chung, Daniel R. Gossett, and Dino Di Carlo. "Three Dimensional, Sheathless, and High-Throughput Microparticle Inertial Focusing Through Geometry-Induced Secondary Flows". In: *Small* 9.5 (Mar. 2013), pp. 685–690.

[27] Daniel R. Gossett and Dino Di Carlo. "Particle Focusing Mechanisms in Curving Confined Flows". In: *Analytical Chemistry* 81.20 (Oct. 2009), pp. 8459–8465.

[28] John Oakey et al. "Particle focusing in staged inertial microfluidic devices for flow cytometry". In: *Analytical Chemistry* 82.9 (2010), pp. 3862–3867.

[29] Gregory Goddard et al. "Ultrasonic particle-concentration for sheathless focusing of particles for analysis in a flow cytometer". In: *Cytometry Part A* 69A.2 (Feb. 2006), pp. 66–74.

[30] Soojung Claire Hur, Henry Tat Kwong Tse, and Dino Di Carlo. "Sheathless inertial cell ordering for extreme throughput flow cytometry." In: *Lab on a chip* 10.3 (2010), pp. 274–280.

[31] Brian K. McKenna et al. "A parallel microfluidic flow cytometer for high-content screening". In: *Nature Methods* 8.5 (May 2011), pp. 401–403.

[32] Menake E. Piyasena et al. "Multinode acoustic focusing for parallel flow cytometry". In: *Analytical Chemistry* 84.4 (Feb. 2012), pp. 1831–1839. arXiv: `NIHMS150003`.

[33] Y. J. Fan et al. "Three dimensional microfluidics with embedded microball lenses for parallel and high throughput multicolor fluorescence detection". In: *Biomicrofluidics* 7.4 (July 2013), p. 044121.

[34] Thomas Blasi et al. "Label-free cell cycle analysis for high-throughput imaging flow cytometry". In: *Nature Communications* 7 (Jan. 2016), p. 10256.

[35] Meiai Lin et al. "Label-free light-sheet microfluidic cytometry for the automatic identification of senescent cells". In: *Biomedical Optics Express* 9.4 (Apr. 2018), p. 1692.

[36] Jian Chen et al. "Microfluidic Impedance Flow Cytometry Enabling High-Throughput Single-Cell Electrical Property Characterization". In: *International Journal of Molecular Sciences* 16.12 (Apr. 2015), pp. 9804–9830.

[37] Michel Godin et al. "Measuring the mass, density, and size of particles and cells using a suspended microchannel resonator". In: *Applied Physics Letters* 91.12 (Sept. 2007), p. 123121.

[38] William J Polacheck and Christopher S Chen. *Measuring cell-generated forces: A guide to the available tools*. 2016.

[39] Eric M. Darling and Dino Di Carlo. "High-Throughput Assessment of Cellular Mechanical Properties". In: *Annual Review of Biomedical Engineering* 17.1 (Dec. 2015), pp. 35–62.

[40] Paul A Janmey and Christopher A McCulloch. "Cell mechanics: integrating cell responses to mechanical stimuli." In: *Annual review of biomedical engineering* 9 (2007), pp. 1–34.

[41] Christophe Guilluy et al. "The Rho GEFs LARG and GEF-H1 regulate the mechanical response to force on integrins." In: *Nature cell biology* 13.6 (June 2011), pp. 722–7.

[42] Kendra D. Nyberg et al. "The physical origins of transit time measurements for rapid, single cell mechanotyping". In: *Lab on a Chip* 16.17 (2016), pp. 3330–3339.

[43] Dian Huang et al. "High-Speed Live-Cell Interferometry: A New Method for Quantifying Tumor Drug Resistance and Heterogeneity". In: *Analytical Chemistry* 90.5 (Mar. 2018), pp. 3299–3306.

[44] R. D. Gonzalez-Cruz, V. C. Fonseca, and E. M. Darling. "Cellular mechanical properties reflect the differentiation potential of adipose-derived mesenchymal stem cells". In: *Proceedings of the National Academy of Sciences* 109.24 (June 2012), E1523–E1529.

[45] Tom Bongiorno et al. "Mechanical stiffness as an improved single-cell indicator of osteoblastic human mesenchymal stem cell differentiation." In: *Journal of biomechanics* 47.9 (June 2014), pp. 2197–204.

[46] Meredith E Fay et al. "Cellular softening mediates leukocyte demargination and trafficking, thereby increasing clinical blood counts." In: *Proceedings of the National Academy of Sciences of the United States of America* 113.8 (Feb. 2016), pp. 1987–92.

[47] G. Bao and S. Suresh. "Cell and molecular mechanics of biological materials". In: *Nature Materials* 2.11 (Nov. 2003), pp. 715–725.

[48] M Radmacher et al. "From molecules to cells: imaging soft samples with the atomic force microscope." In: *Science (New York, N.Y.)* 257.5078 (Sept. 1992), pp. 1900–5.

[49] R M Hochmuth. "Micropipette aspiration of living cells." In: *Journal of biomechanics* 33.1 (Jan. 2000), pp. 15–22.

[50] Dongping Qi et al. "Screening cell mechanotype by parallel microfiltration". In: *Scientific Reports* 5 (Dec. 2015), p. 17595.

[51] Kerryn Matthews et al. "Microfluidic deformability analysis of the red cell storage lesion." In: *Journal of biomechanics* 48.15 (Nov. 2015), pp. 4065–72.

[52] Gonghao Wang et al. "Microfluidic cellular enrichment and separation through differences in viscoelastic deformation". In: *Lab on a Chip* 15.2 (2015), pp. 532–540.

[53] Tobias Sawetzki et al. "Viscoelasticity as a biomarker for High-throughput flow cytometry". In: *Biophysical Journal* 105.10 (2013), pp. 2281–2288.

[54] Josephine Shaw Bagnall et al. "Deformability-based cell selection with downstream immunofluorescence analysis". In: *Integrative Biology (United Kingdom)* 8.5 (2016), pp. 654–664.

[55] Yi Zheng et al. “Recent advances in microfluidic techniques for single-cell biophysical characterization”. In: *Lab on a Chip* 13.13 (2013), pp. 2464–2483.

[56] Jason P Beech et al. “Sorting cells by size, shape and deformability.” In: *Lab on a chip* 12.6 (2012), pp. 1048–1051.

[57] Oliver Otto et al. “Real-time deformability cytometry: on-the-fly cell mechanical phenotyping”. In: *Nature Methods* 12.3 (2015).

[58] Aline T. Santoso et al. “Microfluidic cell-phoresis enabling high-throughput analysis of red blood cell deformability and biophysical screening of antimalarial drugs”. In: *Lab on a Chip* 15.23 (Dec. 2015), pp. 4451–4460.

[59] D. R. Gossett et al. “Hydrodynamic stretching of single cells for large population mechanical phenotyping”. In: *Proceedings of the National Academy of Sciences* 109.20 (May 2012), pp. 7630–7635.

[60] Henry T K Tse et al. “Quantitative diagnosis of malignant pleural effusions by single-cell mechanophenotyping.” In: *Science translational medicine* 5.212 (Nov. 2013), 212ra163.

CHAPTER 2

High-throughput Physical Phenotyping of Cell Differentiation

Jonathan Lin, Donghyuk Kim, Henry T. Tse, Peter Tseng, Lillian Peng, Manjima Dhar, Saravan Karumbayaram, Dino Di Carlo

In this chapter, we present multiparameter deformability cytometry (m-DC), in which we explore a large set of parameters describing the physical phenotypes of pluripotent cells and their derivatives. m-DC utilizes microfluidic inertial focusing and hydrodynamic stretching of single cells in conjunction with high-speed video recording to realize high-throughput characterization of over 20 different cell motion and morphology-derived parameters. Parameters extracted from videos include size, deformability, deformation kinetics, and morphology. We train support vector machines (SVMs) that provide evidence that these additional physical measurements improve classification of induced pluripotent stem cells (iPSCs), mesenchymal stem cells (hMSCs), neural stem cells (hNSCs), and their derivatives compared to size and deformability alone. Additionally, we utilize visual interactive Stochastic Neighbor Embedding (viSNE) to visually map the high-dimensional physical phenotypic spaces occupied by these stem cells and their progeny and the pathways traversed during differentiation. This report demonstrates the potential of m-DC for improving understanding of physical differences that arise as cells differentiate and identifying cell subpopulations in a label-free manner. Ultimately, such approaches could broaden our understanding of subtle changes in cell phenotypes and their roles in human biology.

2.1 Introduction

Cell physical properties, including the shape, size, and resistance of cells to an applied load, stem from other structural and molecular cell properties in a complex fashion that is not easily discerned.[1–4] Compared to conventional molecular biomarkers, these physical properties integrate many molecular changes. Recent findings have clearly demonstrated that physical and mechanical properties can be a promising alternative for phenotyping a range of cell types in different stages. For example, a recent study identified that the differentiation potential of mesenchymal stromal/stem cells is strongly dependent upon their elastic and viscoelastic properties.[5] Similarly, it was shown that cell mechanical markers can be a promising alternative for predicting osteogenesis of differentiating stem cells.[6] Other work has demonstrated that physical changes are important for explaining natural phenomena such as leukocyte demargination.[7]

Obtaining quantitative and reliable measurements of mechanical properties from a large population of cells has always been a challenge.[8] The conventional approaches have been atomic force microscopy (AFM) or micropipette aspiration (MA),[9,10] both of which provide a reliable measurement of the effective Young's modulus of individual cells. However, both methods are time and labor intensive (tens of cells per hour), posing challenges for examining large populations of cells to either obtain statistically valid conclusions or identify rare sub-populations. Recent advances in micro-/nano-fabrication technologies have opened up a range of new mechanophenotyping technologies that can measure deformations of tens to hundreds of cells per second.[11–19] We recently reported a technology, called deformability cytometry, in which a cross-slot microfluidic channel is employed to generate a hydrodynamic extension zone where individual cells are exposed to uniform hydrodynamic stress and deformed.[20] Using a standard inverted microscope setup equipped with a high-speed camera, the technology successfully monitored cell size and deformation at a throughput of approximately 2,000 cells per second. The developed technology, with cell size and deformability alone, successfully discriminated activated/non-activated leukocytes and identified malignancy in pleural effusion samples;[21] however, it was also noted that there were potentially

other easily extracted parameters (e.g., time dependent deformation and cell morphology) that might provide additional physical phenotypic information about cell type/status. As such, we hypothesized that expanding the analysis to additional physical properties may help to distinguish a spectrum of changes that occur as stem cells differentiate.

We were able to extract additional metrics from high-speed video that yielded repeatable cell type-specific values and distributions. Our results indicate that the additional parameters are important; particularly, the addition of morphological parameters (e.g., surface roughness and cell shape) significantly improved the classification accuracy when comparing induced pluripotent stem cells (iPSCs) vs. retinal pigmented epithelial cells (RPEs), neural stem cells (NSCs) vs. neurons and mesenchymal stem cells (MSCs) vs. osteocytes. In addition, iPSCs and RPEs were found to be the most physically distinguishable cell types, while MSCs and osteocytes were the least distinguishable. All of our results indicate that physical properties are modulated in stem cell differentiation and, thus, may play critical roles in cell physiology and can be used to identify cell populations.

2.2 Materials and Methods

2.2.1 Deformability Cytometry

The microfluidic device used for m-DC has been previously described (Figure 2.1).[20] In brief, traditional soft lithography techniques were used to fabricate polydimethylsiloxane microfluidic chips in which cells are uniformly delivered to an extensional flow region (Figure 2.1). Cell suspensions (approximately 100,000 cells/ml) were injected into the microfluidic chip using a syringe pump. Uniform delivery was achieved using inertial microfluidics with a channel aspect ratio of 2 in order to create two vertically stacked focusing positions (channel dimensions 60 μm x 30 μm, flow rate 750 μl/min). The extensional flow caused cells to deform, and the process of deformation was captured using high-speed bright field photography (approximately 500,000 frames per second).

Automated computer analysis (MATLAB) was then performed to extract physical phe-

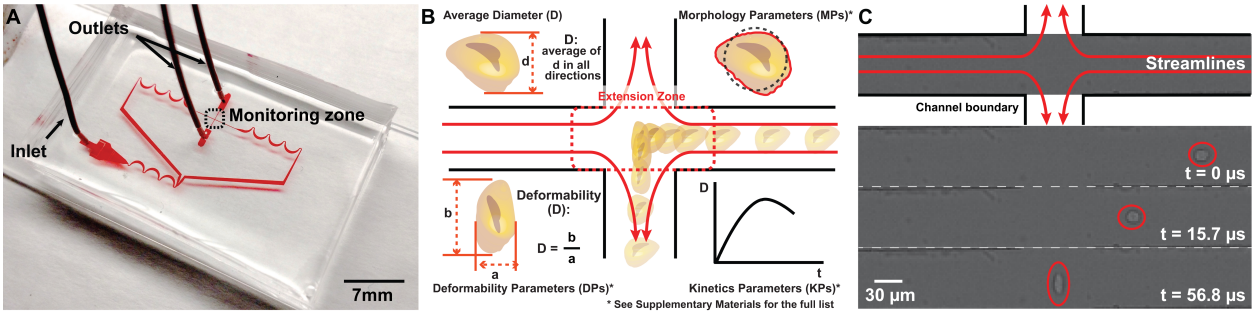

Figure 2.1: Deformability cytometry.
A) Microfluidic device with single inlet and two outlets. Asymmetric focusers and inertial focusing aid in biasing the cells to two vertically stacked equilibrium positions. B) Cells are delivered uniformly to an extensional flow region where they are deformed. The deformation process is captured using high-speed photography, and parameters associated with size, morphology, strain or deformability, and strain rate are extracted from sequences of images through computer automated image analysis. C) Bright field images of a cell entering the extensional flow and deforming.

notype parameters from single cells. Prior to deformation, cell size and morphology were measured. Cell size metrics capture cell diameter and area, with cell area being robust to cell shape. Cell morphology metrics compare the distance from the cell membrane to the cell center ($r_{membrane}$) with a moving average in order to describe the shape and surface roughness of a cell. For these measurements, a radial coordinate system was used to simplify calculations. During the deformation process, cell deformability and deformation kinetics were measured. Deformability captures the peak deformation of each cell normalized by size as an aspect ratio, and the deformation kinetics summarize the aspect ratio changes in the cell as a function of time. The resulting physical phenotype was composed of 21 parameters that fall under the broad categories of cell size, deformability, deformation kinetics and morphology (Figure 2.1b-c, Table 2.1-2.3). General descriptions of the parameters are included in Figure 2.2.

2.2.2 Cell Culture and Preparation for Measurement

Induced pluripotent stem cells (iPSCs, DMD1002) and retinal pigment epithelial cells (RPEs) were obtained through the stem cell core banks at the University of California, Los Angeles

$$Size = \sum_{\theta}^{360^\circ} r_{membrane}(\theta)$$

$$Deformability, D = \frac{l_{vertical}}{l_{horizontal}}$$

$$Morphology = \sum_{\theta=0}^{360^\circ} \left[r_{membrane}(\theta) - \sum_{\phi=\theta-n}^{\theta} r_{membrane}(\phi) \right]$$

$$Kinetics = \sum_{t} D(t) - D(t-1)$$

Figure 2.2: Physical phenotype parameters.

(Eli & Edythe Broad Center of Regenerative Medicine & Stem Cell Research), a funded research facility of the California Institute of Regenerative Medicine (CIRM). The iPSCs were derived from a punch biopsy from the normal human skin of a single patient, and details regarding the generation, culture, and characterization of the iPSCs have been previously published.[22] Retinal pigment epithelial cells (RPEs) were derived from DMD1002 iPSCs at passage 6. DMD1002 iPSCs were plated in suspension in low-adherent dishes with 14% knockout serum replacement (KSR) and 10 mM nicotinamide and cultured for 2 weeks. Then, activin A (final concentration of 140 ng/mL) and fibroblast growth factor (FGF, final concentration of 20 ng/mL) were added into the culture media, and cells were allowed to further grow for an additional 3-4 weeks. Later, pigmented regions of the embryoid bodies were manually dissected using a scalpel under a microscope and re-plated as adherent cultures in RPE media (Alpha DMEM supplemented with 4% FBS, 0.02 ng/ml triiodothyronine, 0.02 μg/ml hydrocortisone, 0.25 mg/ml taurine, 10 mM nicotinamide, non-essential amino acids, N1, 0.1 mM beta-mercaptoethanol and Glutamax).23 Pigmented monolayers of cells were passaged both enzymatically and mechanically and plated at a density of 10,000 cells/cm^2 (Figure 2.5). Cultured cells were trypsinized for 3 minutes (0.025% trypsin, Sigma-Aldrich, Missouri, USA) and resuspended in PBS prior to measurement.

Neural stem cells derived from iPSCs were acquired from XCell Science, Inc. The NSCs were plated in microplates coated in extracellular matrix (Matrigel, Becton Dickinson, Cali-

fornia, USA). They were cultured in neurobasal medium (Life Technologies, California, USA) supplemented with recombinant human fibroblast growth factor 2 (Stemgent, Massachusetts, USA), B27 supplement (Life Technologies), GlutaMAX (Life Technologies), non-essential amino acids (Life Technologies) and 1% penicillin/streptomycin (Life Technologies). Cells were seeded at an initial density of 100,000 cells per cm^2 and allowed to grow for 5 days with a passage on day 3 (Figures 2.6 and 2.7). Cells were released from the surface for measurement using Accutase (Life Technologies) for 3-5 minutes until the cells were visibly detached. NSCs were then resuspended in growth medium for 30 minutes at room temperature prior to beginning the measurement.

Pre-differentiated neurons derived from iPSCs were acquired from XCell Science (California, USA). Neurons were plated on microplates coated with poly-L-ornithine (Sigma-Aldrich) and mouse laminin (Thermo Fisher Scientific, California, USA) at a density of 50,000 cells per cm^2. They were cultured in proprietary medium supplied by XCell Science, Inc. for 5 days (Figures 2.6 and 2.7). Cells were released from the microplate for measurement using Accutase (Life Technologies) for approximately 5 minutes until the cells were visibly detached. The neurons were then resuspended in growth medium for 30 minutes at room temperature prior to measurement.

Human adipose-derived stem cells (hMSCs, Thermo Fisher Scientific) were cultured in tissue culture flasks in MesenPRO RS medium (Thermo Fisher Scientific). Three separate vials of cells were purchased, each derived from a single donor and received at passage number 1. Cells were seeded at approximately 5000 cells per cm^2 and were allowed to grow for 17 days. Cells were released for measurement using TrypLE Express (Thermo Fisher Scientific) for approximately 7 minutes. hMSCs were resuspended in growth medium for 30 minutes at room temperature prior to measurement. The effect of m-DC measurements on hMSC viability and differentiation was also evaluated (Figures 2.8-2.9). Additionally, the batch-to-batch variation of hMSCs was assessed using DC (three vials of hMSCs were compared with data pooled from three technical replicates per sample, Figure 2.11).

Human osteocytes were derived from hMSCs using the StemPro Osteogenesis Differen-

tiation Kit (Thermo Fisher Scientific). hMSCs were initially seeded as previously described and allowed to grow for 7 days in MesenPRO RS medium. They were then placed in Osteogenesis Differentiation Medium for 10 days. Cells were released for measurement using TrypLE Express for approximately 7 minutes. Osteocytes were then resuspended in growth medium for 30 minutes at room temperature before measurement.

2.2.3 Evaluation of Parameter Importance with an Iterative Support Vector Machine (SVM) Approach

To evaluate the importance of each physical parameter, SVMs were trained to classify iPSCs vs. RPEs, NSCs vs. neurons, and MSCs vs. osteocytes. Each of these comparisons represents a differentiated cell type and a pluripotent progenitor. In brief, an SVM is a supervised machine-learning algorithm that defines a boundary based on training data to classify data points into one of two categories. Here, we use SVMs as a tool to determine if physical parameters enable us to classify cells into separate categories (or classes).

Initially, the SVMs were provided with two parameters, cell diameter and maximum deformation. This established a baseline accuracy based on metrics previously measured by deformability cytometry. Next, a new set of SVMs were trained on the full physical phenotype dataset. The improvement in classification accuracy represents the cellular information captured by the new physical phenotype parameters. In each case, SVMs were trained on labeled populations of each cell type and then tested against a 1:1 unlabeled mixture of the two cell types. The classification accuracy was therefore defined as the percentage of cells that were correctly identified during the SVM test.

To evaluate the relative importance of different parameters, SVMs were incrementally trained, adding one parameter at a time. The training began with average cell diameter and maximum deformation, metrics collected by the original deformability cytometry system. From there, the parameters were added to the SVM sequentially to maximize classification accuracy. At each step in this process, a new set of SVMs were trained, each with the parameters selected in previous iterations as well as one of the remaining parameters. The

addition of a remaining parameter that led to the best performance for the new SVM was then included in the next iteration. In this way, parameters that were more important for classifying the cells were added sooner in the process. This process quantitatively revealed the order in which parameters provide new independent information for distinguishing between the two cell types.

In all cases, a grid search was performed on a random subset of the data (500 data points from each cell population) to determine optimal training parameters (radial basis function kernel). Classification accuracy was determined by performing a five-fold cross validation training on a random subset of the data (5000 data points from each cell population).

2.2.4 Visualization of Physical Phenotypes

A two-dimensional projection of the physical phenotype is produced using visual interactive Stochastic Neighbor Embedding (viSNE), an algorithm that reduces dimensionality while preserving spatial relationships between data points.[23] This analysis was performed on iPSCs, NSCs, and neurons, three cell types that represent points along the spectrum of differentiation. A two-dimensional projection allows for the visualization of relationships between cell types and the changes in physical phenotype that occur during differentiation. Further exploration of the differences in physical phenotype between the cell types was performed by relabeling the projections using a parameter from each of the four broad categories of physical phenotypic parameters. Relabeling the projections in this way helped to reveal changes in physical phenotype that occur during differentiation as well as the variability among cells of the same type.

2.3 Results

We first investigated the repeatability and robustness of the new metrics extracted from the high-speed videos of cell deformation. We found that similar to the previously introduced deformability and size (Figure 2.3a), metrics of morphology and deformation kinetics pos-

sessed similar characteristics run to run, independent of slight changes in lighting and flow conditions. For NSCs, the median max deformability had a mean of 1.85 and a coefficient of variance (cv) of 0.15 across nine replicates (3 technical replicates from 3 separate biological replicates). The average median cell size was 13.1 μm with a cv of 0.69. The surface roughness morphology parameter had an average median value of 141.4 and a cv of 0.14. The average relaxation rate, a deformation kinetics parameter, was the least reproducible with a mean value of -0.09 with a cv of 0.21 (Table 2.4).

To investigate the utility in identifying a cell state with these additional parameters beyond deformability and size, SVMs were trained with the full physical phenotype or with only cell size and maximum deformation. In each case, SVMs that were trained with the full physical phenotype outperformed those trained with only size and deformation (Figure 2.3b). The improvements to classification accuracy were not uniform and depended on the comparison populations. The comparison that benefited the most from the addition of new physical phenotype parameters was NSCs vs. neurons, with a 14-percentage point improvement, followed by iPSCs vs. RPEs, with a 13.5-percentage point improvement. The improvement for the comparison of hMSCs vs. osteocytes was the smallest at 4.8 percentage points. In each of the comparisons, the data represented pooled results from three or more biological replicates each with three or more technical replicates.

As shown above, m-DC generates high-dimensional information from individual cells; despite its benefits, data interpretation and decision making from multi-dimensional data can be challenging. As such, we adopted viSNE to visualize the physical phenotypes of iPSCs, NSCs, and neurons without deteriorating the power of single cell analysis (Figure 2.4). viSNE utilizes a t-distributed stochastic neighbor embedding algorithm to generate a scatter plot using all pairwise distances in a high dimensional data set; as such, viSNE provides a biaxial scatter plot that best preserves the projection of the multidimensional physical phenotypic space at a single-cell level. The resulting projection shows that the three cell types occupy generally separable spaces, with some overlap. iPSCs showed the smallest degree of overlap with the other cell populations. NSCs and neurons exhibited a

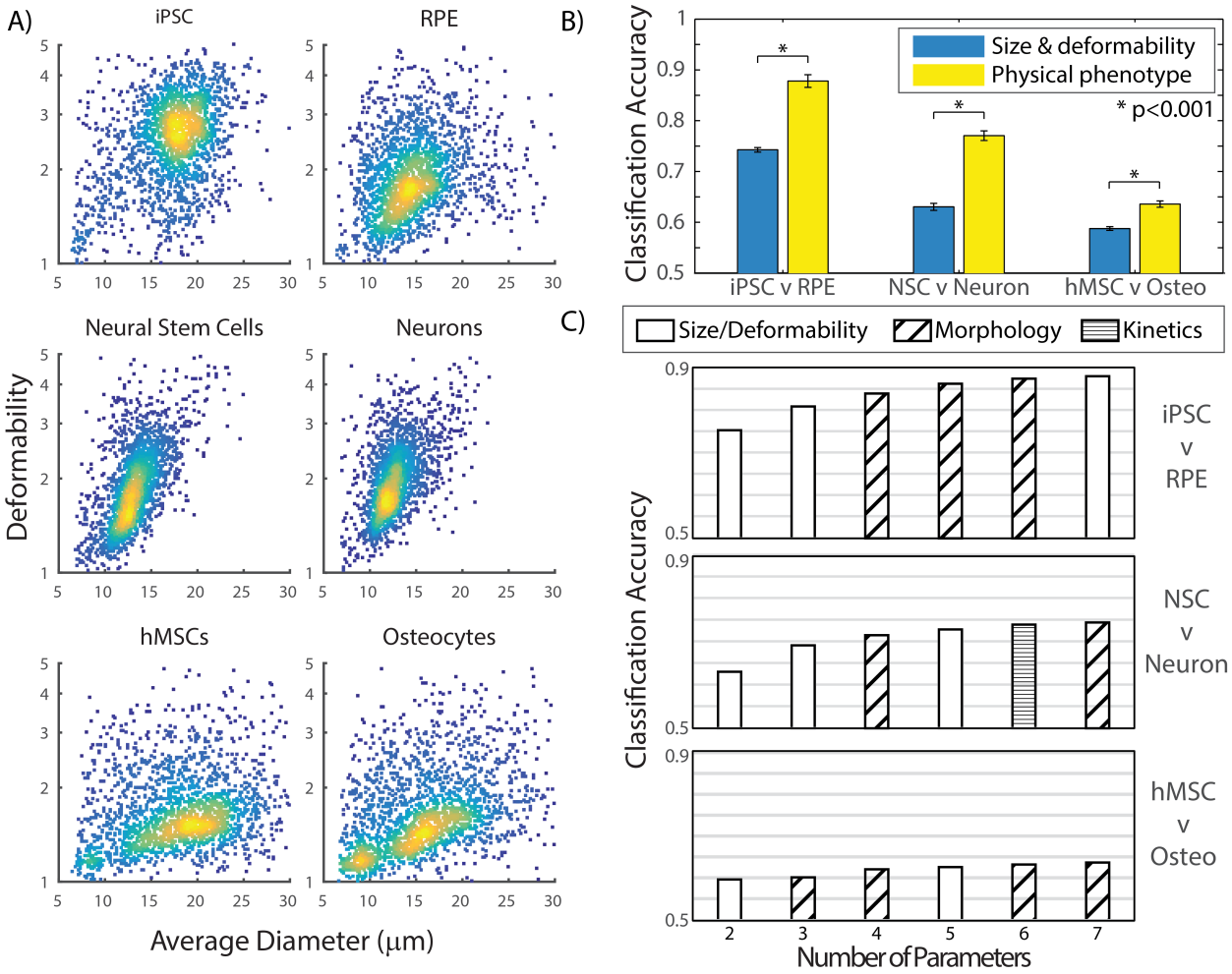

Figure 2.3: Cell classification improves with morphology and kinetics parameters. A) Scatter plots of cell size and deformability for induced pluripotent stem cells (iPSC), retinal pigmented epithelial cells (RPE), neural stem cells (NSC), neurons, mesenchymal stem cells (hMSC), and osteocytes. Each pairing (iPSC/RPE, NSC/Neuron, hMSC/Osteocyte) represents a differentiated cell type and its progenitor stem cell. In the cases of NSCs vs. neurons and hMSCs vs. osteocytes, there are not clear changes in cell size and deformability, suggesting that classification of these cell types based on these parameters alone would be difficult. N=5000 for each scatter plot. B) Classification accuracies of support vector machines (SVMs) trained on each of the three cell type pairs. In each case, SVMs were supplied with either the full physical phenotype or just size and deformability. In all cases, the addition of parameters improved classification accuracy. C) SVMs were trained starting with size and deformability followed with the sequential addition of five additional parameters from the four categories (size, deformability, morphology, and kinetics parameters). The parameters are listed from left to right in order of importance in improving classification accuracy in a cumulative manner. In all cases, SVMs were trained using 5000 randomly sampled cells of each cell type.

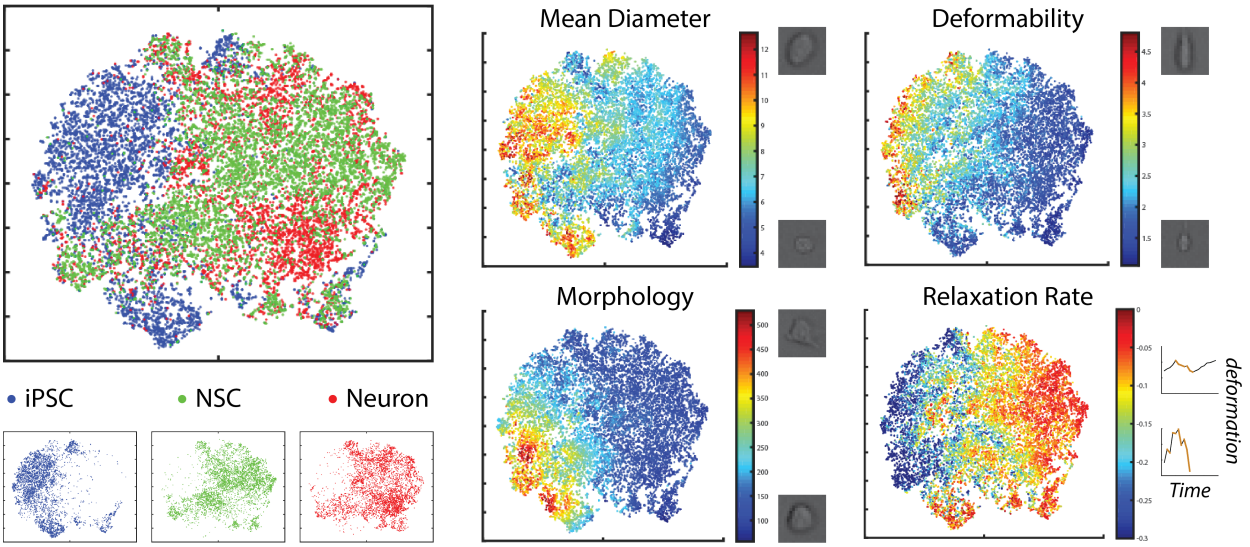

Figure 2.4: Visualization of physical phenotypic spaces occupied by iPSCs, NSCs, and neurons based on their 21 parameters.
A) viSNE is used to produce a two-dimensional projection of the physical phenotypic space. These cells represent different points on the spectrum of differentiation. Separation in this projection indicates differences in physical phenotype. B) The 2-D projection from (A) recolorized according to a parameter from cell size, deformability, deformation kinetics or morphology. The resulting scatter plots demonstrate how these physical properties differ within cell populations and how they change during the differentiation process.

higher degree of overlap, though there were still spaces uniquely occupied by cells in either population.

By relabeling the viSNE projection using a parameter from each of the four broad categories (size, deformability, morphology, and kinetics), a connection to physical changes between the cells during differentiation can be better discerned. This reveals general characteristics of the cell populations and changes that occur during differentiation. In general, iPSCs are larger and more deformable than the more differentiated NSCs and neurons. Additionally, iPSCs have a higher average relaxation rate and higher surface roughness than the other cell populations (Figure 2.4). Comparing NSCs and neurons, we can see differences as well. NSCs are larger and less deformable than neurons with higher surface roughness and lower average rates of relaxation.

2.4 Discussion

m-DC improves upon the previously published deformability cytometry system by expanding the parameters extracted by our analysis algorithm to include morphology and deformation kinetics metrics in addition to new cell size and deformability metrics. The new parameter set, the physical phenotype of a cell, consists of 19 new parameters for a total of 21. We demonstrated that the new metrics contain useful information by measuring the physical phenotypes of several pluripotent cells and their differentiated descendants. We then used the physical phenotypes to train SVMs that revealed that the new parameters improve the classification of these cell types in comparison to SVMs trained only on average cell diameter and maximum deformation. The improvement in classification accuracy indicates that the new parameters capture biologically relevant information that can aid in the identification of these cell populations. It is worth noting that although the classification accuracy increased across all of the cell comparisons, the improvements were not uniform and were cell-type dependent.

The highest observed cell classification accuracy was 87.4% with iPSCs and RPEs. Although the accuracy is not yet high enough for confident determination of all cells in a mixed cell population, our results indicate the potential of the m-DC tool for identifying pluripotent cells within a population of more differentiated cells such as neural stem cells or retinal pigment epithelial cells, and the approach may be more generally applicable to the characterization of the level of remaining pluripotent cells remaining in other cultures, especially given the unique biophysical features for these very phenotypically plastic cells.

We also performed sequential training of SVMs to determine which five parameters were most useful in improving classification accuracy in each comparison. Not surprisingly, the five parameters that emerged as most important in each comparison were dependent on cell type.

We discovered that morphological parameters and additional deformability metrics were generally important in improving accuracy; however, kinetics parameters were less so, only

improving classification between NSCs and neurons. We ranked the physical phenotype parameters by incrementally increasing the number of parameters supplied to an SVM and instructing the SVM to select the parameter that best improved classification at each iteration. This analysis revealed that morphologic parameters as well as new size and deformability measurements were important in improving classification accuracy for most cell populations (Figure 2.3c, Table 2.5). New size parameters compute the cell area instead of the cell diameter, which can be affected by differences in cell morphology such as shape. Thus, the new size parameters may be able to more accurately capture the differences in cell size that can be seen in Figure 2.3. The new deformability parameters also corrected for cell morphology by measuring the increase in the aspect ratio during the deformation process relative to the aspect ratio prior to deformation instead of using a circle as the baseline reference. Additionally, a kinetics parameter, the mean relaxation rate, was useful in improving the classification of NSCs and neurons but was not one of the top five metrics that added additional information beyond deformability and size for classification for the other cell types tested.

Case-specifically, in the comparison between iPSCs and RPEs, the important parameters were morphology and size metrics. The morphology parameters encompass both surface roughness and cell shape, and the size metrics evaluate the area of a cell instead of the previously used size parameter (average diameter). Morphology parameters compare the actual distance from the cell membrane to the cell centroid as a function of radial angle with the moving average of the distance. The surface roughness parameters use a short moving average (5 degrees), and the cell shape parameters use a longer moving average (30 degrees). The importance of the surface roughness and cell shape parameters indicates that there are important differences in both of these types of morphologies between the two cell populations, perhaps due to cortical actin differences, which lead to more ruffling or blebbing. Additionally, it is likely that the area measurements capture the size of iPSCs better when the irregular shape of the cells interferes with diameter measurements.

In the comparison between NSCs and neurons, the important parameters also included

cell area, surface roughness, and cell shape. Notably, the important parameters also included a deformation kinetics parameter, the average relaxation rate. The kinetics parameters are computed based on the cell aspect ratio as a function of time during the deformation process. Increases in the aspect ratio are recorded as deformations, while decreases are recorded as relaxations. Thus, the importance of the average relaxation rate metric indicates that the time-dependent characteristics of the deformation process contain important information about cell phenotypes. It should be noted that this time-dependent metric was found to have a larger inter-trial measurement variation as discussed above with a cv up to 2-3-fold higher than that for deformability measures, which may be one reason for the reduced importance compared to that of the other metrics in the classification of cells.

Lastly, the comparison between hMSCs and osteocytes benefited as well from cell area, surface roughness and cell shape. Interestingly, a morphology parameter that examines the aspect ratio of the cell prior to deformation was also important. This serves as another measurement of cell shape and indicates that morphology is an important distinguishing factor for these cell types.

The analysis of each of these comparisons indicates that some physical phenotype parameters such as cell area and morphology are very important factors in cell classification. However, the differences in each comparison, such as the use of a kinetics parameter in the NSC vs. neuron comparison, reveals that there is no essential set of physical parameters that defines cell types and that many of the different physical phenotype parameters have the potential for being important factors in cell classification. A hallmark of neuron differentiation is the development of a polarized cell structure with axons and dendrites. Studies have shown that the neural differentiation process involves significant reorganization of the cytoskeleton including actin, intermediate filaments, and microtubules.[24,25] A key biomarker for neural stem cells is nestin, an intermediate filament protein whose expression is tightly regulated during differentiation.[26] Furthermore, microtubule organization is particularly important both for maintaining the polarized structure of neurons as well as facilitating their activity.[27,28] These changes to cytoskeletal structure may contribute to the observed decrease

in deformability of NSCs and neurons relative to iPSCs as well as the observed importance of cell morphology when classifying NSCs and neurons (Figure 2.3).

Previous work on hMSCs and osteogenesis has demonstrated that cytoskeletal changes occur during the differentiation process. Pronounced cell shape changes occur, mediated in part by extensive reorganization of actin into thick bundles at the cell periphery.[29,30] Additionally, previous work has also demonstrated that MSCs undergo changes in mechanical properties such as Young's modulus during osteogenesis, although the nature of the change can be method dependent.[31,32] These changes in cell shape due to actin reorganization may help explain the differences in cell morphology observed in m-DC (Figure 2.3). The ambiguous results of previous mechanical measurements comparing hMSCs and osteocytes may also help explain the relative unimportance of deformability when distinguishing the two cell types.

There have been studies demonstrating changes in expression of several genes and transcription factors (e.g., cathepsin D, Pax 6, calbindin, PKC-a, and Mitf) during pluripotent stem cell differentiation;[33,34] many of these contribute to the organization of the cytoskeleton through microfilaments, intermediate filaments, and/or microtubules.[35–42] For example, up-regulation of Pax6 or PKC-a during differentiation may stabilize the cytoskeleton.[43,44] Furthermore, loosely organized heterochromatin and/or abundant euchromatin modifications have been observed in pluripotent cells compared to that observed in differentiated cells.[45–50] These changes to cytoskeletal and nuclear structure may contribute to the decrease in deformability and overall change in physical phenotype observed in RPEs compared to that in iPSCs (Figure 2.3).

Further improvements to the measurement of physical phenotype can be made in the future by focusing on decoupling the effects of cell size on deformability and deformation rate parameters. In the previously described SVM experiments, size information was provided to the SVMs so that deformability and kinetics could be considered in the context of cell size. However, direct comparisons of cell deformability and kinetics will benefit from correcting for cell size.

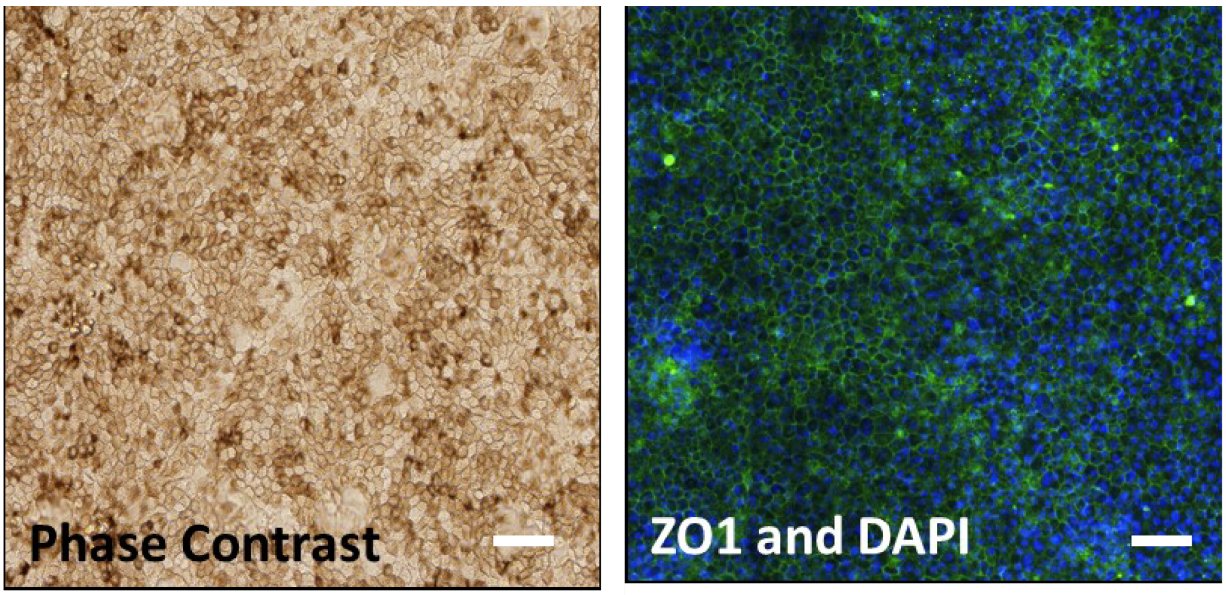

Figure 2.5: Retinal pigmented epithelial (RPE) cell characterization.
Phase contrast images showed the normal pigmented structure of a RPE monolayer. RPEs were immunostained for tight junction protein, ZO1 (using rabbit anti-ZO1, Invitrogen, shown in green) which is a common marker for RPEs, and their nuclei (4',6-diamidino-2-phenylindole or DAPI shown in blue in). The procedure is as follows: a monolayer of RPE cells were fixed in 4% paraformaldehyde (PFA) for 15 minutes and permeabilized with 0.1% triton X-100 for 10 minutes. Cells were blocked in 10% goat serum. Scale bar: 100 μm.

Finally, the visualization of the physical phenotypes of iPSCs, NSCs, and neurons revealed that the three cell types occupy generally separable spaces, confirming that changes in physical phenotype occur throughout the differentiation process. Further exploration revealed changes in all four broad categories of physical parameters. Thus, we have used m-DC to begin the process of mapping the physical changes that occur during differentiation. A general trend found in moving along the spectrum from less to more differentiated was increasing stiffness and more circular cell shapes in suspension. This may be linked to higher cortical tension, and these maps can be useful in understanding the process of differentiation and the importance of physical properties. They can also aid in the detection of subpopulations and provide context to physical changes that occur in other biological processes such as neoplasia.

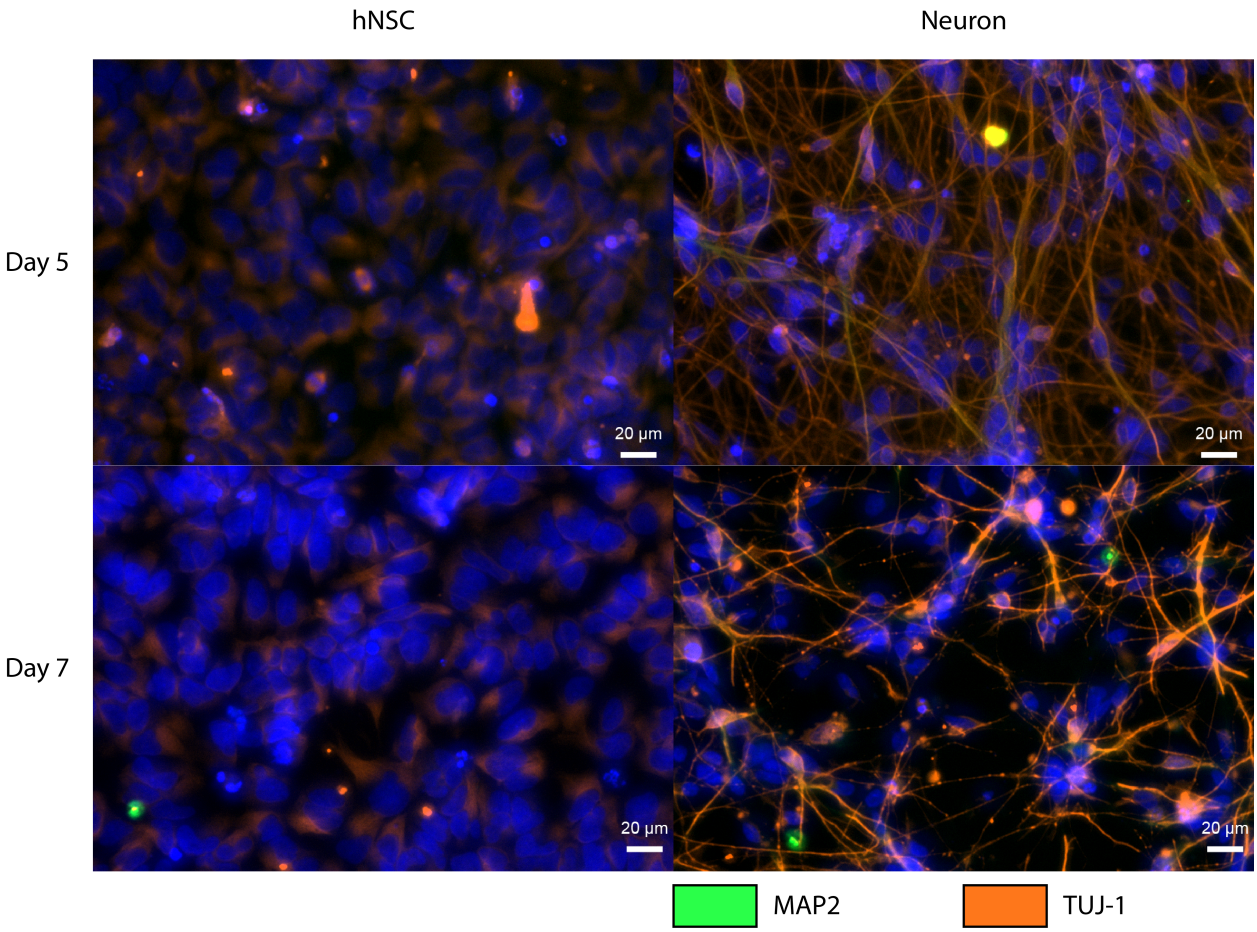

Figure 2.6: Human neural stem cells (hNSCs) and neurons stained using immunohistochemistry for neural markers.
hNSCs and neurons were fixed in 0.2% paraformaldehyde for 10 minutes, permeabilized in 0.04% Triton X-100 for 10 minutes, and immuno-stained with anti-MAP2 (EMD Millipore MAB5326A4, Massachusetts, USA) and anti-TUJ-1 (Abcam ab18207, Cambridge, UK), two neural cell markers. 5% goat serum was used as a blocking agent. Neurons at 5 and 7 days post-plating show high levels of TUJ-1 expression and demonstrate clear neural morphology with extensive neural processes. Nuclear staining was performed with DAPI (Thermo Fisher).

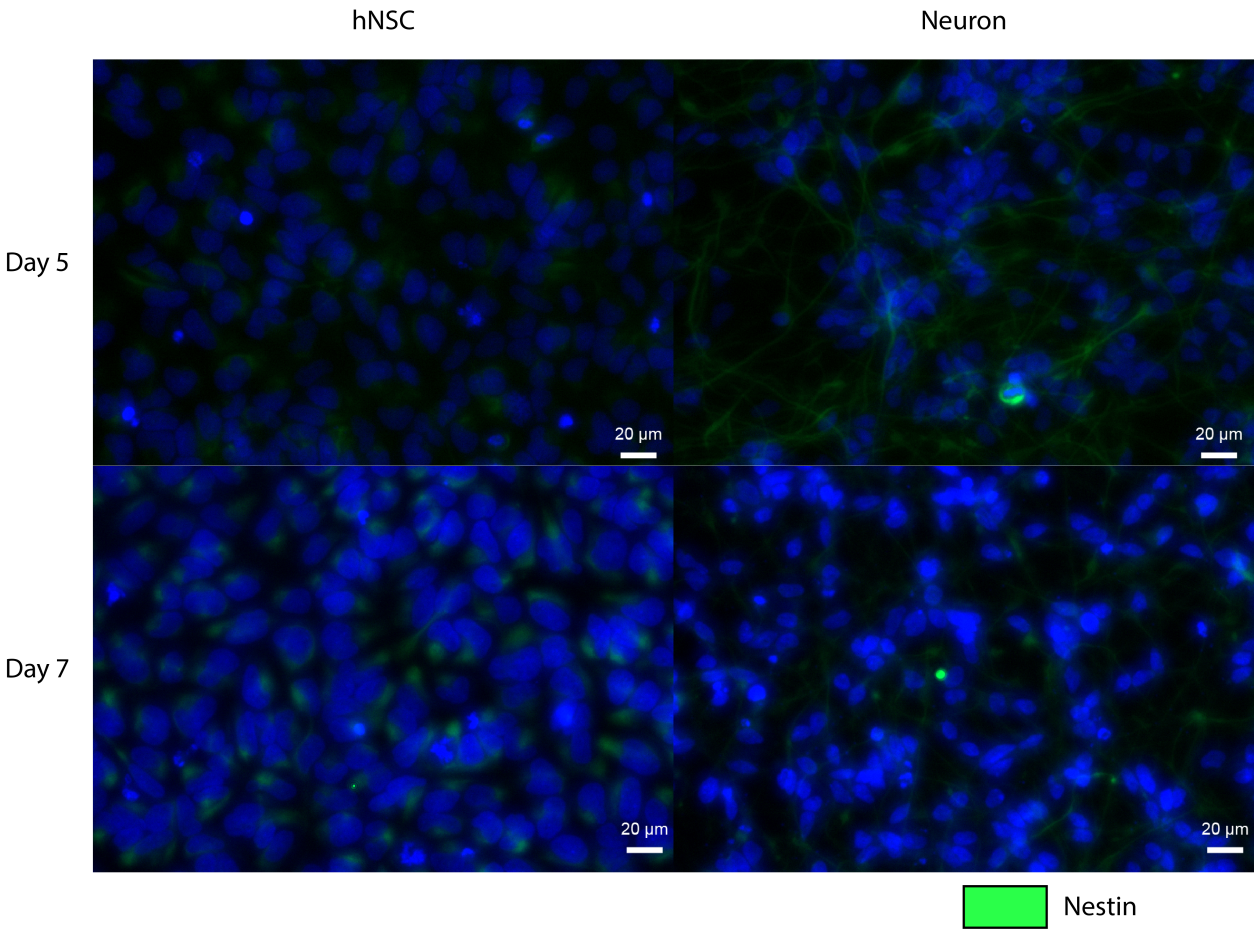

Figure 2.7: hNSCs and neurons stained for nestin
hNSCs and neurons were fixed, permeabilized, and immuno-stained with anti-nestin (EMD Millipore clone 10C2 MAB5326A4) a neural stem cell marker. hNSCs at 5 and 7 days following seeding show nestin expression. Neurons at day 5 show nestin expression with clear neural morphology and neurons at day 7 show decreasing levels of nestin expression. Nuclear staining was performed with DAPI (Thermo Fisher).

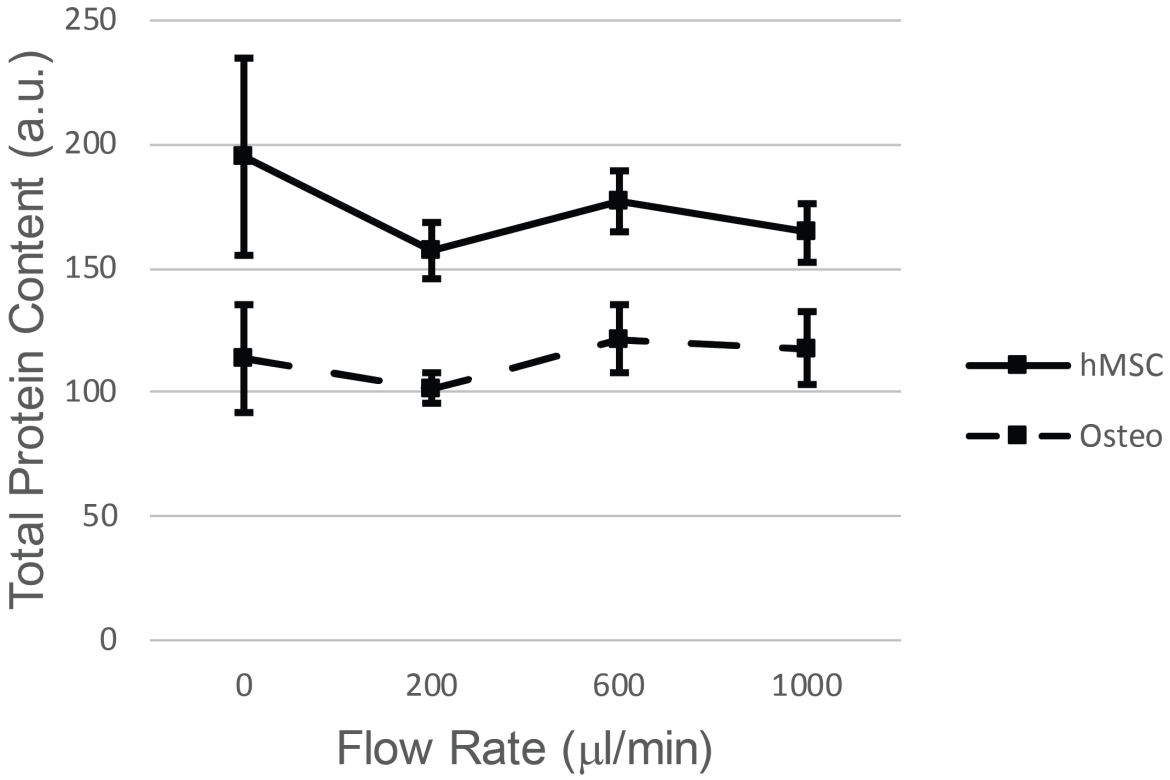

Figure 2.8: hMSC and osteocyte viability 1 week following DC measurements. hMSCs were run through the DC device at varying flowrates to determine the effect of DC on cell viability. Samples with flowrates of 0 μl/min were not exposed to stretching or any flow. Following treatment, the cells were seeded at equal density and kept in either MesenPRO RS medium or osteogenic medium for 1 week. After 1 week, a BCA assay (Pierce, California, USA) was performed to determine total protein concentration which was used as a proxy for cell viability and proliferation. There is no clear effect of DC treatment on hMSC viability. Each datapoint represents 4 replicates and error bars represent a single standard deviation.

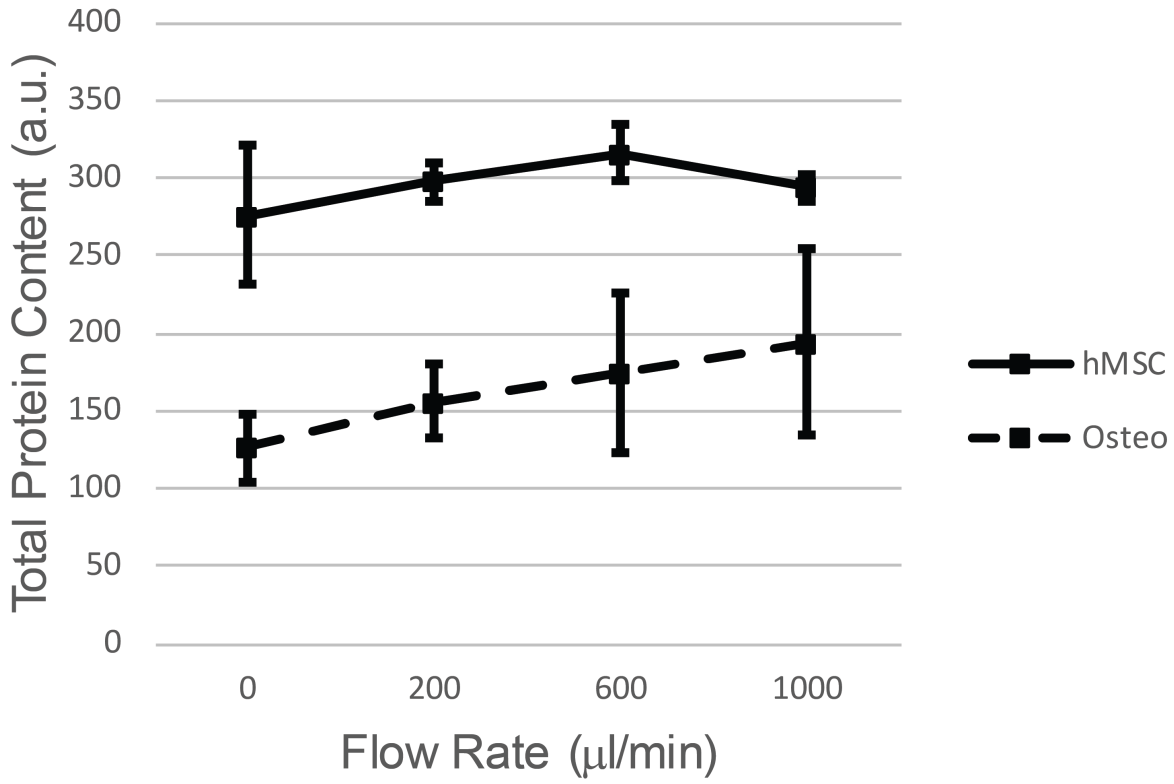

Figure 2.9: hMSC and osteocyte viability 2 weeks following DC measurement. hMSCs were treated as described in Figure 2.8. After 2 weeks, a BCA assay (Pierce) was performed to determine total protein concentration which was used as a proxy for cell viability and proliferation. There is no clear effect of DC treatment on hMSC viability. Each datapoint represents 4 replicates and error bars represent a single standard deviation.

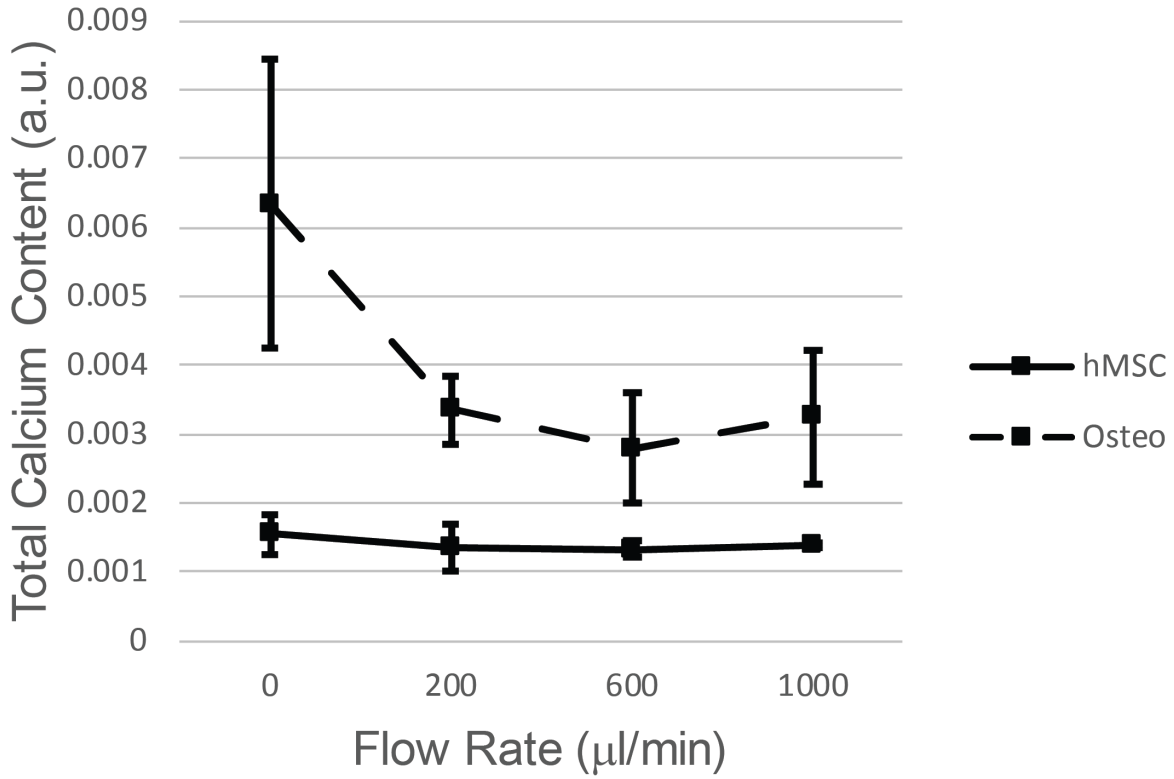

Figure 2.10: hMSC and osteocyte calcium content 2 weeks following DC measurement. Calcium content, an osteogenesis marker, was assayed (QuantiChrom, BioAssay Systems, California, USA) and normalized against total protein content at 2 weeks for the hMSCs and osteocytes described in Figure 2.9. There is no clear effect of DC treatment on the differentiation of hMSCs. Error bars represent 1 standard deviation.

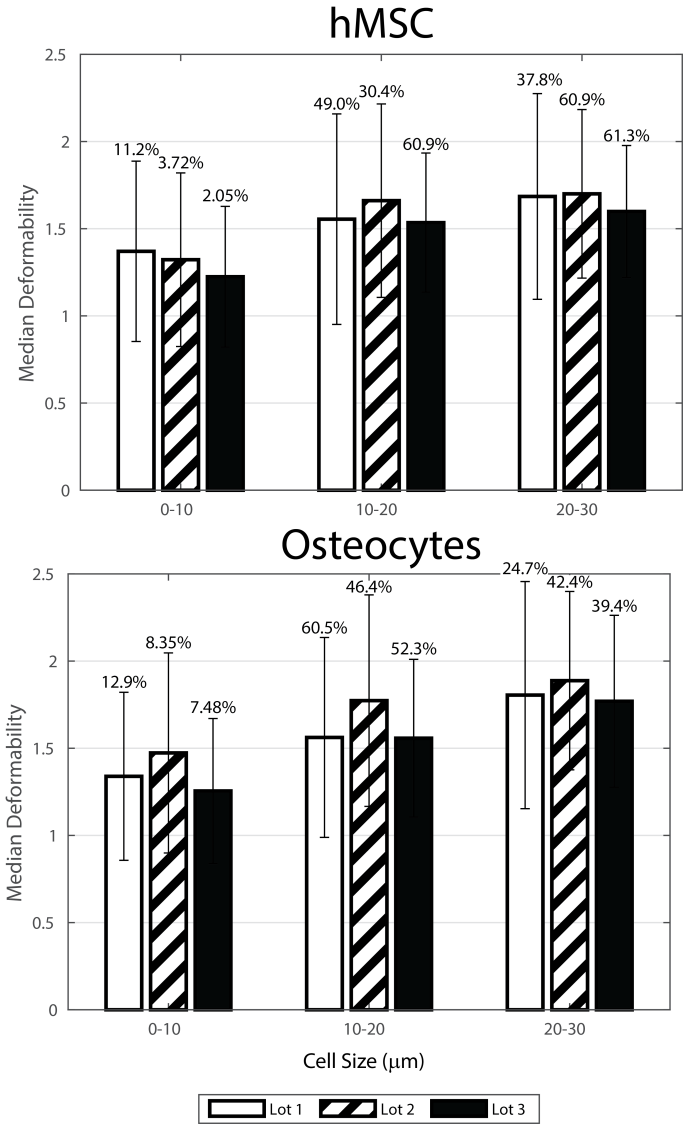

Figure 2.11: Lot variation in hMSCs.
Three batches of adipose-derived stem cells were purchased from Thermo Fisher and measured with several replicates using DC. Here, the median deformability is plotted as a function of cell size for both hMSCs and the osteocytes that were differentiated from them. Error bars represent a standard deviation and numbers above bars represent the percentage of cells that fall within the size range. Although cells within a given size range have similar deformability across multiple batches of hMSCs, the percentage of cells that fell within the size bins varied between batches. Over 20,000 events were collected for each batch of hMSCs. This demonstrates the ability to detect batch-to-batch variation in stem cell properties that is enabled by high-throughput, single-cell measurements.

Table 2.1: Size and Deformability Parameters

Parameter	Description
Average Size	The average cell diameter is computed for each frame prior to the beginning of the deformation process. For each frame, the cell boundary is detected and the diameter is measured in the vertical direction by taking the average of 61 diameters between the angles 60 to 120 degrees, each separated by 1 degree of rotation. These average diameters are then averaged again.
Area	The cell boundary is detected for each frame prior to the beginning of the deformation process. The distance from the cell boundary to the cell centroid is computed as a function of angle with 360 data points each separated by 1 degree of rotation. The sum of these distances is computed and averaged over all pre-deformation frames.
Area2	The cell boundary is detected for each frame prior to the beginning of the deformation process. The distance from the cell boundary to the cell centroid is computed as a function of angle with 360 data points each separated by 1 degree of rotation. The distance data is then smoothed using first order Savitzky-Golay filter with a window size of 17. The resulting data is converted back to Cartesian coordinates and the area of the cell is determined using MATLAB's polyarea function.
Initial aspect ratio	Peak aspect ratio of the cell prior to the deformation process. Aspect ratio is defined as the long axis of the cell divided by the short axis of the cell. The two axes are defined such that one is vertical (between 70 and 110 degrees) and one is horizontal (between -20 and 20 degrees).
Final aspect ratio	Peak aspect ratio of the cell during the deformation process.
Compensated aspect ratio	Aspect ratio measurement that attempts to control for non-unity cell aspect ratio prior to deformation. Compensated aspect ratio is the difference between the final aspect ratio and the initial aspect ratio.

Table 2.2: Morphology Parameters

Parameter	Description
Morphology 1A, 2A, 3A	The cell boundary is detected for each frame prior to the beginning of the deformation process. The distance from the cell boundary to the cell centroid is computed as a function of angle with 360 data points each separated by 1 degree of rotation. This yields cell radius as a function of angle which is used to compute a moving average of length 5, 15, or 30 degrees. The moving average is subtracted from the raw radius data and the absolute value of the result is integrated over the entire cell (360 degrees).
Morphology 1C, 2C, 3C	For these morphology parameters, the moving average is compared to the raw cell data and the number of cross over events between the two functions is counted.
Cell size and morphology	Combined measurement of surface roughness and cell size. Prior to deformation, cell diameter is measured in the vertical direction (between 60 to 120 degrees). Additionally, the distance from the cell boundary to the cell centroid is computed as a function of angle with 360 data points each separated by 1 degree of rotation. The cell diameter is then added to the sum of the absolute value of the derivative of the cell boundary distance.

Table 2.3: Deformation Kinetics Parameters

Parameter	Description
Max, initial, average deformation rate	Cell aspect ratio is recorded as a function of time during the deformation process. This function is differentiated to produce the rate of aspect ratio change as a function of time. These parameters represent the maximal positive rate of aspect ratio change, the first recorded positive rate of aspect ratio change, and the average of all recorded positive rate of aspect ratio change, respectively.
Max, initial, average relaxation rate	These parameters represent the maximal negative rate of aspect ratio change, the first recorded negative rate of aspect ratio change, and the average of all recorded negative rate of aspect ratio change, respectively.
Deformation rate before max	This parameter represents the positive rate of aspect ratio change that occurs just prior to the maximum measured aspect ratio.
Wobble	A second order polynomial is fit to the rate of change of aspect ratio and the root mean square of the residuals is reported.

Table 2.4: Technical and biological variability in measurements of neural stem cells. This table compares the variability due to the m-DC system with the biological variability of neural stem cells. The first three rows of the table contain the coefficients of variance for the average median values of 4 physical phenotype parameters for each of 3 biological replicates. Each statistic represents the results of 3 technical replicates and gives an estimate of the variability of the m-DC measurement itself. The final row of the table contains the coefficients of variance for the average median values of the same parameters for the overall dataset. Each statistic describes the results of 3 biological replicates and gives an estimate of the biological variability of neural stem cells.

Biological Replicate	Deformability CV	Cell Size CV	Surface Roughness CV	Relaxation Rate CV
1	0.015	0.009	0.018	0.013
2	0.032	0.010	0.021	0.070
3	0.013	0.003	0.037	0.039
All	0.167	0.079	0.158	0.237

Table 2.5: Repeatability of relative importance of physical phenotype parameters. This table depicts three replicates of the SVM-based experiments to determine the relative importance of physical phenotype parameters. In these experiments, SVMs were initially supplied with average cell size and deformability. From there, parameters were iteratively added to the SVM, maximizing the improvement of classification accuracy at each iteration (see Materials and Methods). Replicates of these experiments demonstrate that some parameters are robustly important for distinguishing certain pairings of cells (e.g. cell area for iPSC vs. RPE) while other parameters are seemingly interchangeable (e.g. Morphology M3A and M3C in iPSC vs. RPE). This confirms that parameters can often be correlated and that there is not a clear minimum set of parameters capable of describing all cell types.

iPSC vs. RPE	3	4	5	6	7
Replicate 1	Area	Cell Size & Morphology	Morphology: M1A	Morphology: M3A	Area 2
Replicate 2	Area	Morphology: M1C	Morphology M3C	Area 2	Compensated Aspect Ratio
Replicate 3	Area	Morphology: M1C	Cell Size & Morphology	Morphology: M1A	Morphology: M3A
NSC vs. Neuron					
Replicate 1	Area 2	Morphology: M3A	Area	Average Relaxation Rate	Cell Size & Morphology
Replicate 2	Area 2	Morphology: M3A	Average Relaxation Rate	Morphology: M1C	Area
Replicate 3	Area 2	Morphology: M3A	Average Relaxation Rate	Area	Morphology: M2A
hMSC vs. Osteocyte					
Replicate 1	Cell Size & Morphology	Morphology: M2A	Area 2	Compensated Aspect Ratio	Morphology: M1A
Replicate 2	Morphology: M2A	Cell Size & Morphology	Morphology: M1A	Morphology: M2C	Average Deformation Rate
Replicate 3	Morphology: M1C	Cell Size & Morphology	Area	Morphology: M3C	Initial Aspect Ratio

2.5 Conclusions

In this report, we demonstrated m-DC, an improvement to the previously described deformability cytometry platform by adding two new categories of physical parameters: cell morphology and deformation kinetics. In conjunction with size and deformability metrics, the new parameters produce a description of a cell's physical phenotype. Using SVMs, we demonstrated that the physical phenotype improves classification of pluripotent stem cells and their differentiated descendants. Additionally, we showed that the new categories of parameters are important contributors to the improved classification accuracy. Finally, we demonstrated how the physical phenotype can be visualized and used to explore the physical changes that occur during the differentiation process. m-DC is a high-throughput and label-free method for analyzing the physical properties of cells. This technique opens the door to label-free assays of differentiation progression with applications in stem cell therapy. Furthermore, the biophysical maps produced by measurements of stem cells and their descendants provide a tool for studying the role of differentiation in other biological processes such as cancer. Ultimately, such approaches can deepen our understanding of subtle changes to cell phenotypes and their implications in physiological processes.

2.6 Acknowledgements

The authors acknowledge financial support from the Packard Foundation and the National Science Foundation grant #1150588. JL is supported under NIH MSTP Training Grant #T32GM008042.

2.7 Conflicts of Interest

D.D., H.T. and the Regents of the University of California have financial interests in CytoVale Inc., which is commercializing the deformability cytometry technology.

2.8 References

[1] Eric M. Darling and Dino Di Carlo. "High-Throughput Assessment of Cellular Mechanical Properties". In: *Annual Review of Biomedical Engineering* 17.1 (Dec. 2015), pp. 35–62.

[2] Paul A Janmey and Christopher A McCulloch. "Cell mechanics: integrating cell responses to mechanical stimuli." In: *Annual review of biomedical engineering* 9 (2007), pp. 1–34.

[3] Christophe Guilluy et al. "The Rho GEFs LARG and GEF-H1 regulate the mechanical response to force on integrins." In: *Nature cell biology* 13.6 (June 2011), pp. 722–7.

[4] Kendra D. Nyberg et al. "The physical origins of transit time measurements for rapid, single cell mechanotyping". In: *Lab on a Chip* 16.17 (2016), pp. 3330–3339.

[5] R. D. Gonzalez-Cruz, V. C. Fonseca, and E. M. Darling. "Cellular mechanical properties reflect the differentiation potential of adipose-derived mesenchymal stem cells". In: *Proceedings of the National Academy of Sciences* 109.24 (June 2012), E1523–E1529.

[6] Tom Bongiorno et al. "Mechanical stiffness as an improved single-cell indicator of osteoblastic human mesenchymal stem cell differentiation." In: *Journal of biomechanics* 47.9 (June 2014), pp. 2197–204.

[7] Meredith E Fay et al. "Cellular softening mediates leukocyte demargination and trafficking, thereby increasing clinical blood counts." In: *Proceedings of the National Academy of Sciences of the United States of America* 113.8 (Feb. 2016), pp. 1987–92.

[8] G. Bao and S. Suresh. "Cell and molecular mechanics of biological materials". In: *Nature Materials* 2.11 (Nov. 2003), pp. 715–725.

[9] M Radmacher et al. "From molecules to cells: imaging soft samples with the atomic force microscope." In: *Science (New York, N.Y.)* 257.5078 (Sept. 1992), pp. 1900–5.

[10] R M Hochmuth. "Micropipette aspiration of living cells." In: *Journal of biomechanics* 33.1 (Jan. 2000), pp. 15–22.

[11] Dongping Qi et al. “Screening cell mechanotype by parallel microfiltration”. In: *Scientific Reports* 5 (Dec. 2015), p. 17595.

[12] Kerryn Matthews et al. “Microfluidic deformability analysis of the red cell storage lesion.” In: *Journal of biomechanics* 48.15 (Nov. 2015), pp. 4065–72.

[13] Gonghao Wang et al. “Microfluidic cellular enrichment and separation through differences in viscoelastic deformation”. In: *Lab on a Chip* 15.2 (2015), pp. 532–540.

[14] Tobias Sawetzki et al. “Viscoelasticity as a biomarker for High-throughput flow cytometry”. In: *Biophysical Journal* 105.10 (2013), pp. 2281–2288.

[15] Josephine Shaw Bagnall et al. “Deformability-based cell selection with downstream immunofluorescence analysis”. In: *Integrative Biology (United Kingdom)* 8.5 (2016), pp. 654–664.

[16] Yi Zheng et al. “Recent advances in microfluidic techniques for single-cell biophysical characterization”. In: *Lab on a Chip* 13.13 (2013), pp. 2464–2483.

[17] Jason P Beech et al. “Sorting cells by size, shape and deformability.” In: *Lab on a chip* 12.6 (2012), pp. 1048–1051.

[18] Oliver Otto et al. “Real-time deformability cytometry: on-the-fly cell mechanical phenotyping”. In: *Nature Methods* 12.3 (2015).

[19] Aline T. Santoso et al. “Microfluidic cell-phoresis enabling high-throughput analysis of red blood cell deformability and biophysical screening of antimalarial drugs”. In: *Lab on a Chip* 15.23 (Dec. 2015), pp. 4451–4460.

[20] D. R. Gossett et al. “Hydrodynamic stretching of single cells for large population mechanical phenotyping”. In: *Proceedings of the National Academy of Sciences* 109.20 (May 2012), pp. 7630–7635.

[21] Henry T K Tse et al. “Quantitative diagnosis of malignant pleural effusions by single-cell mechanophenotyping.” In: *Science translational medicine* 5.212 (Nov. 2013), 212ra163.

[22] Saravanan Karumbayaram et al. “From Skin Biopsy to Neurons Through a Pluripotent Intermediate Under Good Manufacturing Practice Protocols”. In: *STEM CELLS Translational Medicine* 1.1 (Jan. 2012), pp. 36–43.

[23] El Ad David Amir et al. “ViSNE enables visualization of high dimensional single-cell data and reveals phenotypic heterogeneity of leukemia”. In: *Nature Biotechnology* 31.6 (May 2013), pp. 545–552. arXiv: NIHMS150003.

[24] Claudia Compagnucci et al. “Cytoskeletal dynamics during in vitro neurogenesis of induced pluripotent stem cells (iPSCs)”. In: *Molecular and Cellular Neuroscience* 77 (2016), pp. 113–124.

[25] Claudia Compagnucci et al. “The cytoskeletal arrangements necessary to neurogenesis”. In: *Oncotarget* 5.15 (2016).

[26] Jonas Dahlstrand, Michael Lardelli, and Urban Lendahl. “Nestin mRNA expression correlates with the central nervous system progenitor cell state in many, but not all, regions of developing central nervous system”. In: *Developmental Brain Research* 84.1 (1995), pp. 109–129.

[27] Casper C. Hoogenraad and Frank Bradke. “Control of neuronal polarity and plasticity - a renaissance for microtubules?” In: *Trends in Cell Biology* 19.12 (Dec. 2009), pp. 669–676.

[28] Alfredo Cáceres, Bing Ye, and Carlos G. Dotti. “Neuronal polarity: Demarcation, growth and commitment”. In: *Current Opinion in Cell Biology* 24.4 (Aug. 2012), pp. 547–553. arXiv: NIHMS150003.

[29] Gregory Yourek, Mohammad A. Hussain, and Jeremy J. Mao. “Cytoskeletal changes of mesenchymal stem cells during differentiation”. In: *ASAIO Journal* 53.2 (2007), pp. 219–228.

[30] J. Pablo Rodríguez et al. “Cytoskeletal organization of human mesenchymal stem cells (MSC) changes during their osteogenic differentiation”. In: *Journal of Cellular Biochemistry* 93.4 (2004), pp. 721–731.

[31] Pattie S. Mathieu and Elizabeth G. Loboa. "Cytoskeletal and Focal Adhesion Influences on Mesenchymal Stem Cell Shape, Mechanical Properties, and Differentiation Down Osteogenic, Adipogenic, and Chondrogenic Pathways". In: *Tissue Engineering Part B: Reviews* 18.6 (2012), pp. 436–444.

[32] Eric M. Darling et al. "Viscoelastic properties of human mesenchymally-derived stem cells and primary osteoblasts, chondrocytes, and adipocytes". In: *Journal of Biomechanics* 41.2 (2008), pp. 454–464.

[33] Yuchun Tsai et al. "Human iPSC-Derived Neural Progenitors Preserve Vision in an AMD-Like Model". In: *Stem Cells* 33.8 (Aug. 2015), pp. 2537–2549. arXiv: 15334406.

[34] Taku Tanaka et al. "Generation of retinal ganglion cells with functional axons from human induced pluripotent stem cells". In: *Scientific Reports* 5.1 (July 2015), p. 8344.

[35] A S Pollock and H L Santiesteban. "Calbindin expression in renal tubular epithelial cells. Altered sodium phosphate co-transport in association with cytoskeletal rearrangement." In: *The Journal of biological chemistry* 270.27 (July 1995), pp. 16291–301.

[36] Suzanne Carreira et al. "Mitf regulation of Dia1 controls melanoma proliferation and invasiveness". In: *Genes and Development* 20.24 (2006), pp. 3426–3439.

[37] Hiroyuki Kamao et al. "Characterization of human induced pluripotent stem cell-derived retinal pigment epithelium cell sheets aiming for clinical application". In: *Stem Cell Reports* 2.2 (2014), pp. 205–218.

[38] Hoshimi Kanemura et al. "Pigment epithelium-derived factor secreted from retinal pigment epithelium facilitates apoptotic cell death of iPSC". In: *Scientific Reports* 3 (2013), p. 2334.

[39] Lyndsay L. Leach et al. "Induced Pluripotent Stem Cell-Derived Retinal Pigmented Epithelium: A Comparative Study Between Cell Lines and Differentiation Methods". In: *Journal of Ocular Pharmacology and Therapeutics* 32.5 (2016), pp. 317–330.

[40] Caroline Brandl et al. “In-Depth Characterisation of Retinal Pigment Epithelium (RPE) Cells Derived from Human Induced Pluripotent Stem Cells (hiPSC)”. In: *NeuroMolecular Medicine* 16.3 (2014), pp. 551–564.

[41] Yuko Iwasaki et al. “Differentiation/purification protocol for retinal pigment epithelium from mouse induced pluripotent stem cells as a research tool”. In: *PLoS ONE* 11.7 (2016), pp. 1–20.

[42] Liana C. Boraas et al. “Cytoskeletal expression and remodeling in pluripotent stem cells”. In: *PLoS ONE* 11.1 (2016), pp. 1–16.

[43] Robert Hugues Duparc et al. “Pax6 is required for delta-catenin/neurojugin expression during retinal, cerebellar and cortical development in mice”. In: *Developmental Biology* 300.2 (2006), pp. 647–655.

[44] Deanne H Hryciw, Carol a Pollock, and Philip Poronnik. “PKC-alpha-mediated remodeling of the actin cytoskeleton is involved in constitutive albumin uptake by proximal tubule cells.” In: *American journal of physiology. Renal physiology* 288.6 (2005), F1227–35.

[45] Gaoyang Liang and Yi Zhang. “Embryonic stem cell and induced pluripotent stem cell: An epigenetic perspective”. In: *Cell Research* 23.1 (2013), pp. 49–69.

[46] Sarah X L Huang et al. “Efficient generation of lung and airway epithelial cells from human pluripotent stem cells”. In: *Nature biotechnology* 32.1 (2014), pp. 84–91. arXiv: NIHMS150003.

[47] Alexandre Gaspar-Maia et al. “Open chromatin in pluripotency and reprogramming”. In: *Nature Reviews Molecular Cell Biology* 12.1 (2011), pp. 36–47.

[48] Anne-Marie Courtot et al. “Morphological analysis of human induced pluripotent stem cells during induced differentiation and reverse programming.” In: *BioResearch open access* 3.5 (2014), pp. 206–16.

[49] Shinya Yamanaka and Helen M Blau. “Nuclear reprogramming to a pluripotent state by three approaches.” In: *Nature* 465.7299 (2010), pp. 704–12. arXiv: NIHMS150003.

[50] Allyson J. Merrell and Ben Z. Stanger. “Adult cell plasticity in vivo: De-differentiation and transdifferentiation are back in style”. In: *Nature Reviews Molecular Cell Biology* 17.7 (2016), pp. 413–425.

CHAPTER 3

A High-throughput, Inertial-microfluidic, Digital, Radiofrequency-encoded Array (HIDRA) Parallel Flow Cytometer

Jonathan Lin, Dino Di Carlo

Flow cytometry is a powerful biological tool, allowing multiparameter, single-cell measurements of biochemical markers. Although conventional flow cytometers are capable of high-throughput, their sample throughput is limited by serial processing. In this chapter, we demonstrate a high-sample-throughput, inertial-microfluidic, digital radiofrequency-encoded array (HIDRA) parallel flow cytometer that is capable of simultaneous interrogation of eight samples through Fluorescence Imaging using Radiofrequency-tagged Emission (FIRE) and inertial microfluidic focusing. We perform validation with 6-peak fluorescent calibration beads and demonstrate compatibility with conventional biological assays. With this system, we adapt a research tool for high throughput screening, enabling the study of drug-cell interactions at the single cell level.

3.1 Introduction

In recent decades, the standard approach to drug discovery has become increasingly brute force with researchers regularly testing thousands to millions of compounds in search for hits. In this vein, the workhorse of the pharmaceutical industry has been high-throughput screening, a process that utilizes automation and massive parallelization to screen large compound libraries against cell populations of interest. The assays used in high-throughput

screening, such as microplate absorbance measurements, are typically aggregate-readout techniques where the information from large numbers of cells are combined into a single output value.[1]

Drug discovery stands to benefit from high-content assay formats that can provide single-cell multiplexed molecular information that reports on compound mechanisms of action. One widely used assay format has been multi-color fluorescence flow cytometry.[2] Flow cytometry has enabled single cell investigation of numerous drug screening-relevant experiments including antibody screening, efflux transporter activity, receptor binding, G-protein-coupled receptor activity, and in vitro toxicology.[3] However, although these approaches currently are being used extensively, there is a fundamental trade-off between higher information content and sample throughput when using flow cytometry, which has significantly lower throughput than low-content well-plate reader-based assays. Commercial flow cytometry systems sip from a single well at a time and report the ability to process a 384-well plate in 20 minutes. The main approach to increase sample throughput in flow cytometry for drug discovery has been to run smaller sample volumes, sacrificing statistical power and imposing restrictions on experimental design, or to simply run more flow cytometers in parallel, which of course comes with significant cost and complexity barriers.[3–5]

Numerous novel microfluidic technologies have been developed to improve the throughput of flow cytometry. A subset of these technologies improve the spatial distribution of cells, an important parameter to ensure uniform illumination. These technologies enhance flow focusing using inertial or acoustic focusing systems.[6–9] This allows for higher sample flow rates, achieving modest improvements to throughput. Another subset of technologies improve throughput by generating multiple stream of particles, allowing either higher volumetric throughput or parallel interrogation of multiple samples.[10–13] Whereas particle focusing approaches can only achieve minor improvements to throughput, parallelization approaches have the potential to improve throughput by an order of magnitude or more.

There are significant technical challenges, however, in terms of focusing and optically sensing parallel streams of cells that have prevented significant parallelization within a single

instrument and flow cell. Previously, others have explored microfluidic, inertial focusing, and acoustic focusing approaches to generating parallel streams.[8,10–12] Each of the previous systems has had to make significant sacrifices on the optical side of the system due to the difficulty of interrogating multiple spatial locations and efficiently collecting fluorescent emissions across a large field of view. Previous works have explored using scanning laser illumination systems and cameras to overcome these barriers. However, these approaches lack the speed and sensitivity of photomultiplier tube (PMT) based systems and put substantial limits on sample throughput.

Here we introduce the High-throughput, Inertial-microfluidic, Digital Radiofrequency-encoded Array (HIDRA) Flow Cytometer (Figure 3.1). The HIDRA flow cytometer simultaneously addresses the challenges of parallel sample fluid handling and optical readout and analysis, focusing and optically detecting 8 concurrent samples for a total volume throughput exceeding 960 μL/min, all with the sensitivity of a commercial PMT-based flow cytometer across 2 fluorescent channels and 2 scatter channels. The flow cell consists of a microfluidic chip in which 8 syringe pump-driven parallel inertial focusing streams are merged into an imaging window without losing their relative spatial information which encodes the initial sample. In the imaging window the location information of each cell is next encoded through fluorescent imaging using frequency-tagged emission (FIRE).[14] In this system, spatial information is encoded into a frequency-modulated emission or scatter following excitation by a linear laser comb consisting of a gradient of amplitude-modulated excitation beams. The resulting single-cell signals therefore contain both intensity information as well as sample origin-encoding which allows us to assign each cell to its stream of origin. With this system we show that a 6-point IC_{50} dose-response curve can be obtained for a sample all in a single shot.

3.2 Results and Discussion

3.2.1 Spatial Encoding of Samples using Parallel Inertial Focusing

A microfluidic flow cell was fabricated to uniformly deliver 8 samples to a small interrogation region while maintaining spatial separation between the samples.

The first region of the flow cell, the inlet region, consists of 8 fluidic inlets arrange in fan-like pattern (Figure 3.1B). This region of the flow cell acts as an interface between the relatively large input tubings and the small microfluidic channels comprising the next portion of the device, the focusing region.

This next region consists of 8 high aspect ratio channels that inertially focus particles. Here, inertial focusing causes cells to migrate to two vertically stacked position, allowing for uniform illumination of cells in the downstream interrogation region. In brief, inertial focusing occurs when cells in finite Reynolds number flows interact with two opposing forces, the shear gradient and wall lift forces, causing them to migrate to equilibrium positions within the channel. Channels with similar cross sections have been used previously when uniform cell delivery is needed.[10,15–18] An important consideration in the design of the focusing region is the channel length. The channels need to be sufficiently long to allow particles to fully migrate to the equilibrium positions near the midpoints of the channel floor and ceiling. At the same time, the channels need to be short to minimize the fluidic resistance of the flow cell. High fluidic resistance makes it difficult to achieve the driving pressures needed for high volumetric flowrates. A channel length of 5 mm was found to have high inertial focusing efficiency at a wide range of flowrates. Devices were tested by infusing a suspension of Jurkat cells stained with Calcein Red-Orange and performing fluorescent streak imaging (Figure 3.7). At a Reynolds number of 50, the Jurkat cells were focused to the two vertically stacked focusing positions along the channel midlines (Figure 3.1B). This effect was also seen at Reynolds numbers of 100 and 150. Thus, the inertial focusing appears to be robust over a wide range of Reynolds numbers. It is worth noting that these Reynolds numbers correspond to flowrates ranging between 120 and 360 μl per minute per sample, a substantial

improvement over commercially available flow cytometers.

The final region before the flow cell outlet is the interrogation region. This is an imaging region where cells from each sample stream are interrogated. This region is designed as a single, wide channel which serves as a merging point for the 8 sample streams. Here, the challenge is to maintain spatial separation of the samples without the use of channel walls which would scatter light and make side scatter measurements difficult. This is accomplished by once again taking advantage of particle inertia. In finite Reynolds number flows (Re ¿ 1), particle inertia allows particles to migrate across fluid streamlines.[17] Thus, despite the tendency for the fluid to decelerate and spread out to fill the larger imaging region, particles are carried forward by their own momentum. Thus, the spatial separation between sample streams is preserved as seen in Figures 3.1B and 3.7. It is important to note that the vertically stacked focusing positions along the channel midlines are important here as well since they keep particles and cells away from the portions of the flow that are changing direction and decelerating most rapidly. This ensures that particles are uniformly delivered to the illumination spots.

3.2.2 Frequency Encoding of Spatial Information

Interrogation of the 8 sample streams is accomplished using a single laser and a single photodetector for each data channel (forward scatter, side scatter, FITC fluorescence, and PE fluorescence). This is accomplished by structuring the illumination such that each interrogation laser spot is amplitude modulated at a unique frequency. This frequency encoding is present in forward and side scattered light as well as fluorescence emissions (fluorophores serve as receiver broadcasters of the amplitude modulated signal). Therefore, spatial information, i.e. which laser spot a particle is interacting with, is encoded in the frequency domain. This spatial information can be easily extracted using the fast Fourier transform. This imaging technique, Fluorescence Imaging using Radiofrequency-tagged Emission, was previously reported.[14,19,20] In brief, the amplitude modulated laser spots are created by passing a laser through an acousto-optic deflector (AOD) to generate frequency-shifted beams

which can be combined in an interferometer to produce beat-frequency amplitude modulation. The AOD allows for digital control of the illumination, simplifying the process of aligning the laser spots with the microfluidic flow cell.

The ability to identify the sample stream of origin for a given event was demonstrated by flowing 8 unique samples through the flow cell, one sample to each inlet. These samples were generated by selecting 7 unique pairs of beads from the 6 peak calibration bead set. The eighth sample was a blank, containing no beads. Each sample was faithfully reproduced by the cytometer with minimal crosstalk between the different sample streams, confirming the system's ability to detect the steam of origin for each event (Figure 3.2).

3.2.3 Cytometer Characterization

Characterization of the HIDRA system was performed using 6-peak calibration beads, polystyrene particles with 6 discrete concentrations of encapsulated fluorophore. First, a suspension of all 6 beads was infused into all 8 of the sample inlets at a high volumetric flow rate (960 μl/min total throughput). All 6 bead types could be resolved, but each bead had two corresponding, overlapped peaks (Figure 3.3). This observation was caused by subtle differences in illumination and optical collection efficiency across the different flow streams. In order to normalize the fluorescence intensity across flow streams, a Gaussian mixture model was fitted to the brightest bead population in each flow stream. The median intensities were then used to normalize the fluorescence from each stream.

Following the normalization, the 6 peaks are well separated and the computed mean equivalent soluble fluorophore (MESF) metrics are 277 for PE and 709 for FITC (Figures 3.3, 3.4). The high MESF value for FITC is likely due to autofluorescence from the silicone elastomer used in prototyping. The sensitivity of the system is on par with commercially available flow cytometers. Thus, a large sacrifice is fluorescence sensitivity is not necessary to achieve parallel measurements in our system.

In order to evaluate the performance of the fluidic system, we returned to the results from the experiment where 7 unique pairs of beads from the 6 peak calibration set and one

blank sample were infused into the cytometer. The faithful reporudction of all 8 samples indicates that the different samples remain fluidically isolated, demonstrating the ability of the HIDRA system to act as a truly parallel cytometer where distinct samples can be measured simultaneously (Figure 3.2).

3.2.4 Simultaneous 6-point IC_{50} curve

In order to demonstrate compatibility of the HIDRA system with conventional drug screening experiments, two IC_{50} experiments were performed with ethanol and camptothecin as inducers of apoptosis (Figure 3.5, 3.6). In each case, 6 points on an IC_{50} curve and 2 compensation experiments were conducted simultaneously at a total volumetric throughput of 960 μl/min. Each experiment yielded expected results with ethanol having an IC_{50} value near a concentration of 10% v/v (1 hour incubation) and camptothecin having an IC_{50} value between 10 μM and 100 μM (24 hour incubation).

Measuring each treatment condition simultaneously reduces experimental complexity by removing the need to consider measurement time when designing experiments. Additionally, high sample-throughput in conjunction with parallelization removes the need to trade event number, and thus statistical power, for sample throughput. Additionally, it avoids the complexity associated with normalizing results across multiple flow cytometers.

3.3 Materials and Methods

3.3.1 Chip Design and Manufacture

The microfluidic flow cell in the HIDRA system was fabricated using traditional single-layer soft lithography. A silicon wafer was spin-coated with KMPR 1025 (Microchem Corp.) to a layer thickness of 30 micrometers. The flow cell design was transferred to the photoresist using a printed photomask (CAD/Art Services, Inc.) and a mask aligner (Karl Suss). After developing the photoresist, the resultant mold was used to fabricate devices in silicone elastomer (Sylgard 184, Dow Corning). The devices were then bonded to glass slides using

a plasma cleaner (Harrick Plasma).

Cell suspensions are introduced into the flow cell's eight inlets using syringe pumps (Harvard Apparatus). After the inlet region, the 8 separate fluid streams are brought close together into 8 parallel channels (60 μm channel widths with 20 μm channel walls), reducing field of view of requirements for the optical system. The high aspect ratio (AR = 2) of these channels in conjunction with a high Reynolds number (Re ¿ 50) allow them act as inertial focusers that focus particles and cells to two vertically stacked equilibrium positions along channel midlines. Following the inertial focusing region of the device, the 8 sample streams are merged into a single large channel. Here, particle inertia allows particles to cross fluid streamlines, preventing particle migration and maintaining 8 distinct particle streams. Once in the merged channel, the particle streams are interrogated with 8 laser spots in the absence channel walls which would otherwise cause scattering of the laser light. Thus, the flow cell acts to uniformly introduce particles and cells to the interrogation.

3.3.2 Optical System

The HIDRA optical system prototype was supplied by Omega Biosystems. The system utilizes a 1 watt, 488 nm, long coherence length laser (Coherent) coupled with an acousto-optic deflector (Isomet) to generate spatially separated, frequency-shifted light. The signal sent to the acousto-optic deflector (AOD), generated using an arbitrary waveform generator (AWG) (Wavepond), is designed to yield 16 frequency-shifted beams with frequency shifts in the radiofrequency range. These beams are interfered in pairs using an interferometer, taking advantage of beat-frequency amplitude modulation to produce 8 amplitude modulated beams. Each beam is sinusoidally amplitude-modulated at a different frequency, allowing frequency to serve as a unique identifier for each beam. The beams are then imaged onto the flow cell where they are used to interrogate each of the 8 sample streams.

It is worth noting that the AOD-induced frequency shift is entirely controlled by the signal output of the AWG. Thus, the position and beat frequency of each of the 8 excitation beams can be digitally controlled. Additionally, the frequency spacing between the interrogation

spots can be controlled as well, allowing for widely spaced frequencies such that power spreading due to fast moving particles will not cause data to spill over into frequency bins of adjacent interrogation spots.

Transmitted and fluorescent light are gathered using a high numerical aperture lens. The transmitted light is transformed to forward scatter light using a blocker bar and is collected into a photodiode. Fluorescent light is picked off using a dichroic mirror and then passed into two PMTs, each with a band pass optical filter separated by another dichroic mirror. Side-scattered light is also collected into a PMT and used for triggering.

3.3.3 Signal Processing and Data Analysis

Analog signals from the PMTs and photodiode are digitized using a 16-bit, 250 MS/s digitizer (AlazarTech) clocked off of the AWG. The resultant signals are conventional flow cytometry pulses convolved with the amplitude modulation from the illumination system. After digitization of the signal, the fast Fourier transform (FFT) can be used to determine the frequency of the amplitude modulation, and thus the stream of origin, for each event.

The remainder of the data processing pipeline is similar to that of conventional flow cytometry. Pulses are low-pass filtered and then are measured in the time domain to produce measurements such as integrated intensity, pulse height and pulse width. A multiplicative factor, derived from a Gaussian mixture model fit to a calibration experiemnt, is applied to each sample stream in order to compensate for changes in illumination and optical collection efficiency across the field of view. The Gaussian mixture model fitting is further described in system calibration and characterization.

Data is collected in the Metis software package (Omega Biosystems). For conventional flow analysis, the data is exported in FCS 3.0 format and imported into FlowJo (FlowJo, LLC).

3.3.4 System Calibration and Characterization

The sensitivity of the HIDRA system was characterized using 10 μm diameter, 6-peak fluorescent beads (URCP-100-2, Spherotech). This bead suspension consists of beads, each with one of six fluorescent intensities that span a large dynamic range.

For initial calibration and performance characterization, the 6-peak bead suspension was infused into all 8 sample inlets. The sample stream of origin of each event was automatically determined by binning the events based on the frequency with the highest amplitude in the FFT. A Gaussian mixtures model was then applied to the data from each sample stream to identify each of the six bead populations. The resultant models were then used to determine the multiplicative correction factor applied to each sample stream to compensate for decreased collection efficiency at the edges of the field of view. The resulting adjusted data were then used to compute moelcules of equivalent soluble fluorochrome (MESF), a metric of system performance.

Testing of the inertial focusing performance was performed using Jurkat cells stained with Calcein red-orange. Identical cell suspensions were simultaneously infused into each sample inlet at three volumetric flow rates (120, 240, and 360 μl/min). Fluorescent streak images were then performed on a conventional fluorescent microscope (Eclipse Ti-E, Nikon) using a long integration time.

Further testing of the flow cell was performed using 8 unique combinations of fluorescent beads drawn from the 6-peak calibration bead set. A suspension of two out of six bead intensities was infused into each sample inlet with one sample inlet receiving only distilled water. The resulting events were then used to quantify the number of events whose source streams were misidentified.

3.3.5 Cell Culture and Viability Assays

A proof of concept study was performed using ethanol as a means of inducing apoptosis in Jurkat cells. Jurkat cells were treated with varying concentrations of ethanol for one hour

in order to mimic a half maximal inhibitory concentration (IC_{50}) assay. After treatment the cells were stained using an apoptosis kit (V13242, Invitrogen) consisting of FITC-Annexin V, a protein that binds phosphatidylserine which acts as a marker of early apoptosis, and propidium iodide, a membrane impermeant nucleic acid stain that serves as a marker of cell death. Six concentrations of ethanol were assayed in this way and the remaining two sample streams were used for compensation experiments where apoptosis was induced with ethanol but only one of the two cell stains was added. Compensation experiments serve to quantify the spectral overlap of the fluorescent dyes. The spectral overlap is then used to derived multiplicative factors that remove the contribution of spectral overlap from the data. All eight samples were run simultaneously on the HIDRA system with a total volumetric flow rate of 960 μl/min. Compensation and gating were performed using FlowJo.

A similar experiment was performed using camptothecin, a topoisomerase inhibitor. Cells were treated with various concentrations of camptothecin and incubated for 24 hours at 37° C, 5% CO2.

3.4 Conclusions and Future Directions

In this chapter, we have demonstrated a parallel flow cytometry system that utilizes optical and fluidic multiplexing to simultaneously measure 8 samples with a single fluidic and optical system. The instrument represents a significant cost savings and complexity reduction compared to running multiple flow cytometers. Additionally, the instrument does not require a complex, large field of view optical system. Rather, it uses a laser and PMTs, standard flow cytometer components, to perform measurements. The components of this system not traditionally found in flow cytometers represent a small price increase and minimal increase in complexity. The instrument exceeds the volumetric sample throughput of commercially available flow cytometers, sidestepping the need to trade sample throughput for sample volume. Additionally, the ability to run time sensitive experiments such as an IC_{50} in parallel removes the need to account for measurement time, reducing the experimental complexity.

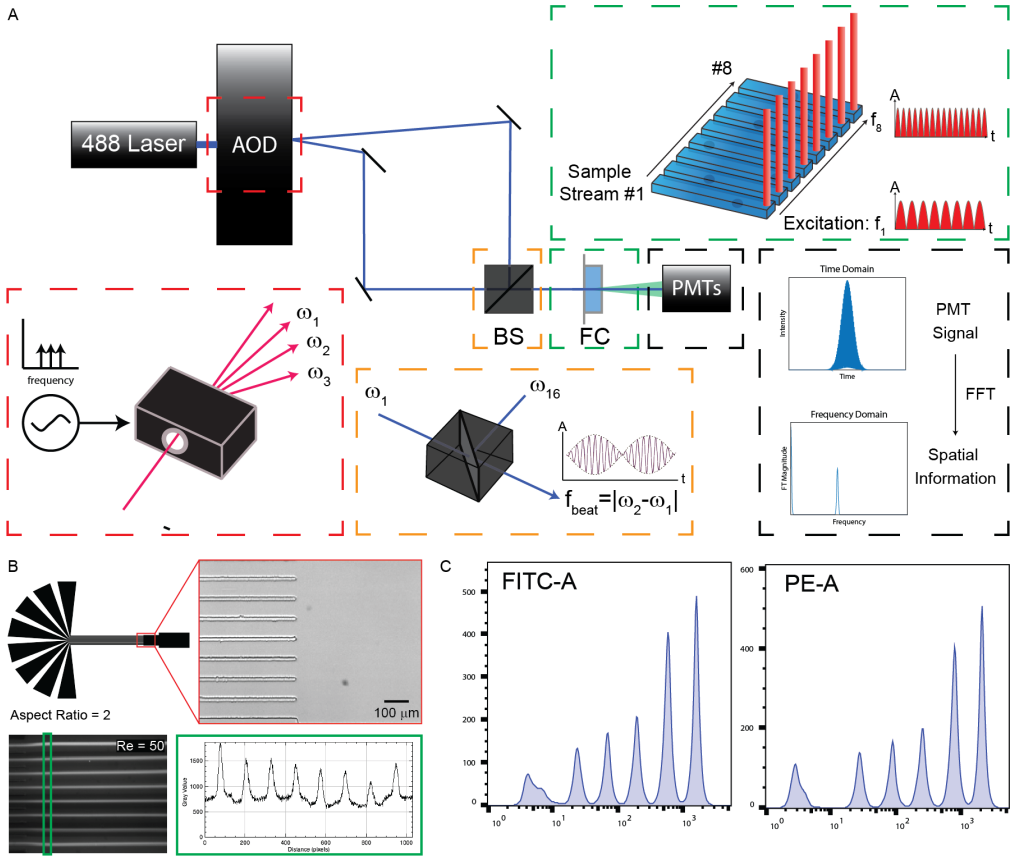

Figure 3.1: System schematic and validation.
A) Optical system. A 488 nm laser passes through an acousto-optic deflector (AOD), generating frequency-shifted beams which are combined in an interferometer to generate amplitude-modulated excitation beams. Each excitation beam illuminates a separate fluid stream in the flow cell (FC). Fluorescent emission and scattered light are measured with photomultiplier tubes (PMT). *Red inset*: An AOD and an arbitrary waveform generator produce 16 digitally-controlled, frequency-shifted beams. *Orange inset*: Frequency-shifted beams are combined with a beam splitter (BS). Interference causes beat frequency amplitude modulation with each beam modulated at a unique frequency. *Green inset*: Eight amplitude modulated beams illuminate eight sample streams. *Black inset*: Example raw data. Events are flow cytometry pulses superimposed with engineered amplitude modulation. The fast Fourier transform (FFT) determines which beam an event originated from. Conventional flow cytometry measurements (e.g. pulse area & height) are performed as normal. B) Microfluidic device. Eight channels inertially focus particles then merge into an interrogation region where samples are illuminated. *Clockwise*: Device schematic, brightfield image of interrogation region, fluorescent streak images of Jurkat cells stained with Calcein Red-Orange (sample throughput = 960 μl/min), and line plot of fluorescence intensity vs. distance corresponding to green region. Inertial focusing localizes cells to channel midlines. C) Fluorescence sensitivity was measured using calibration beads. All 6 peaks were detected in the FITC and PE channels MESF of <700 and <300 respectively.

#	Bead	Bead
1	A	B
2	C	D
3	E	F
4	C	E
5	A	F
6	none	none
7	D	F
8	B	D

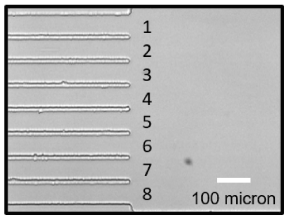

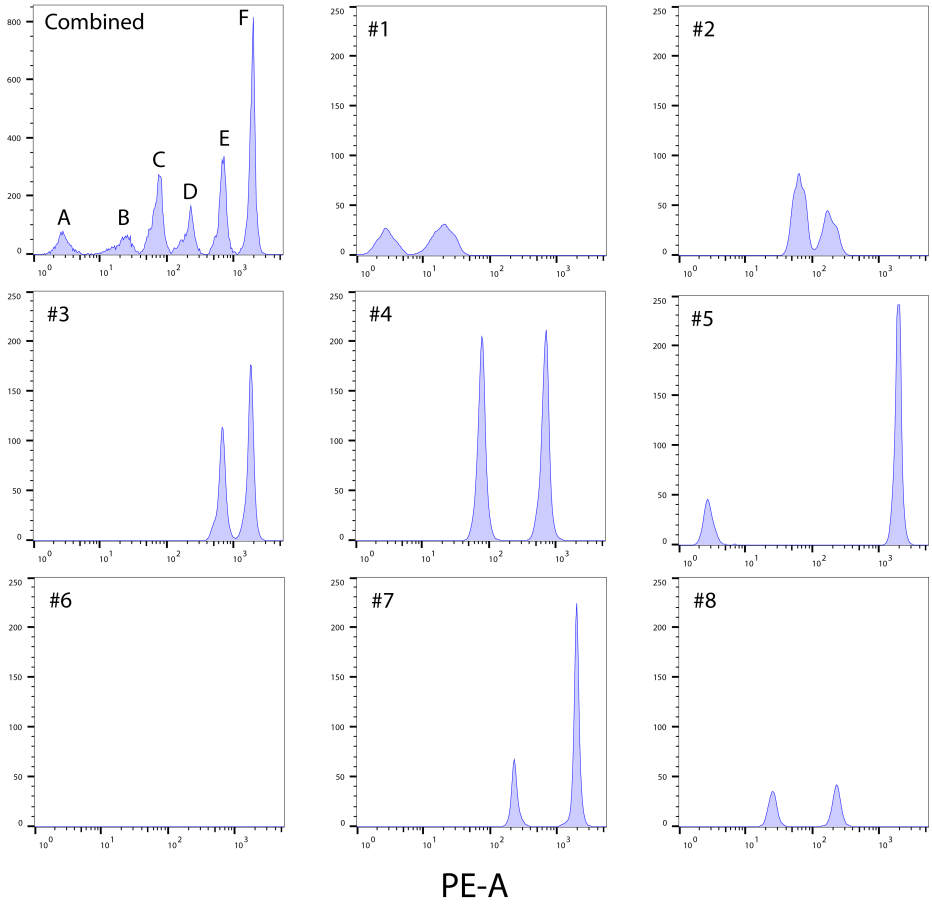

Figure 3.2: Simultaneous measurement of multiple samples.
Eight unique samples were generated by choosing combinations of two bead intensities from the six-peak calibration beads used to characterize the system. *Left*: Legend of sample compositions corresponding to each flow channel. Letters correspond to one of six bead intensities as shown in the upper left histogram. *Right*: Each numbered histogram depicts events collected from one of eight flow channels. All samples were run and interrogated simultaneously and events were assigned automatically using frequency-domain analysis. The upper left histogram is the aggregated data from all eight channels. It is important to note that flow channel 6 was not spiked with any beads.

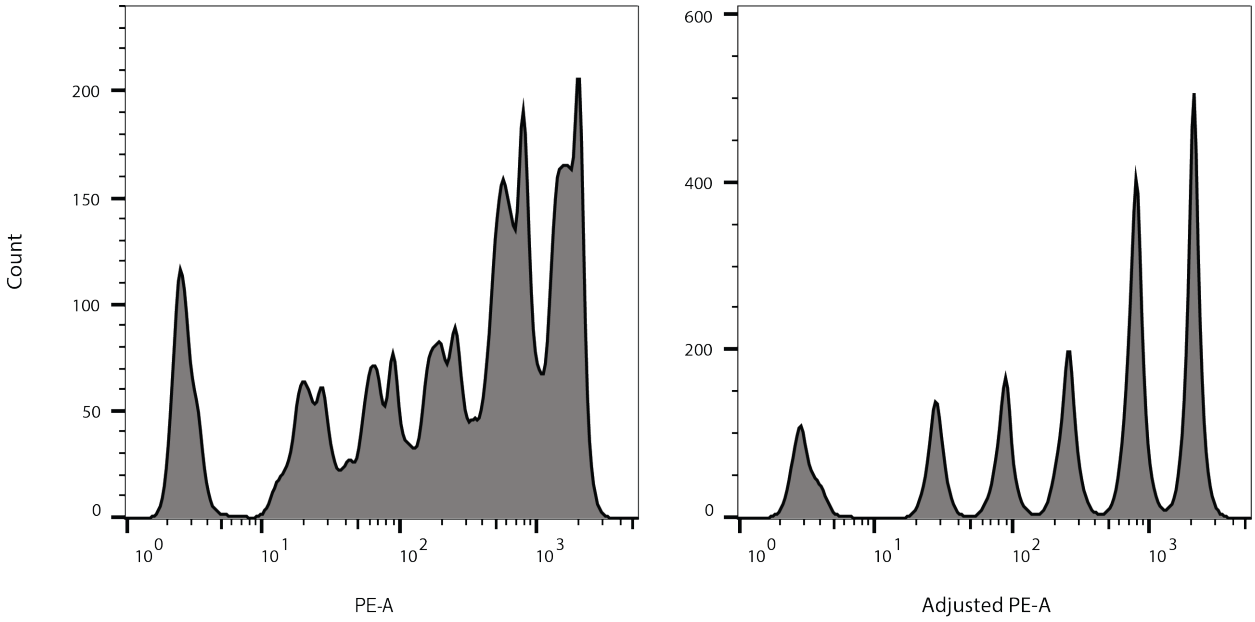

Figure 3.3: Effect of equalization between sample streams.
Left: Integrated fluorescence of 6-peak fluorescent beads prior to detection of sample stream of origin. *Right*: Integrated fluorescence of 6-peak beads following detection of sample stream of origin and application of automated equalization. Equalization corrects for differences in collection efficiency across the field of view and is determined by running 6 peak calibration beads and fitting a six population gaussian mixtures model to each sample stream. The equalization coefficient is set to be the multiplicative scaling factor required to make the means of the highest intensity populations equal.

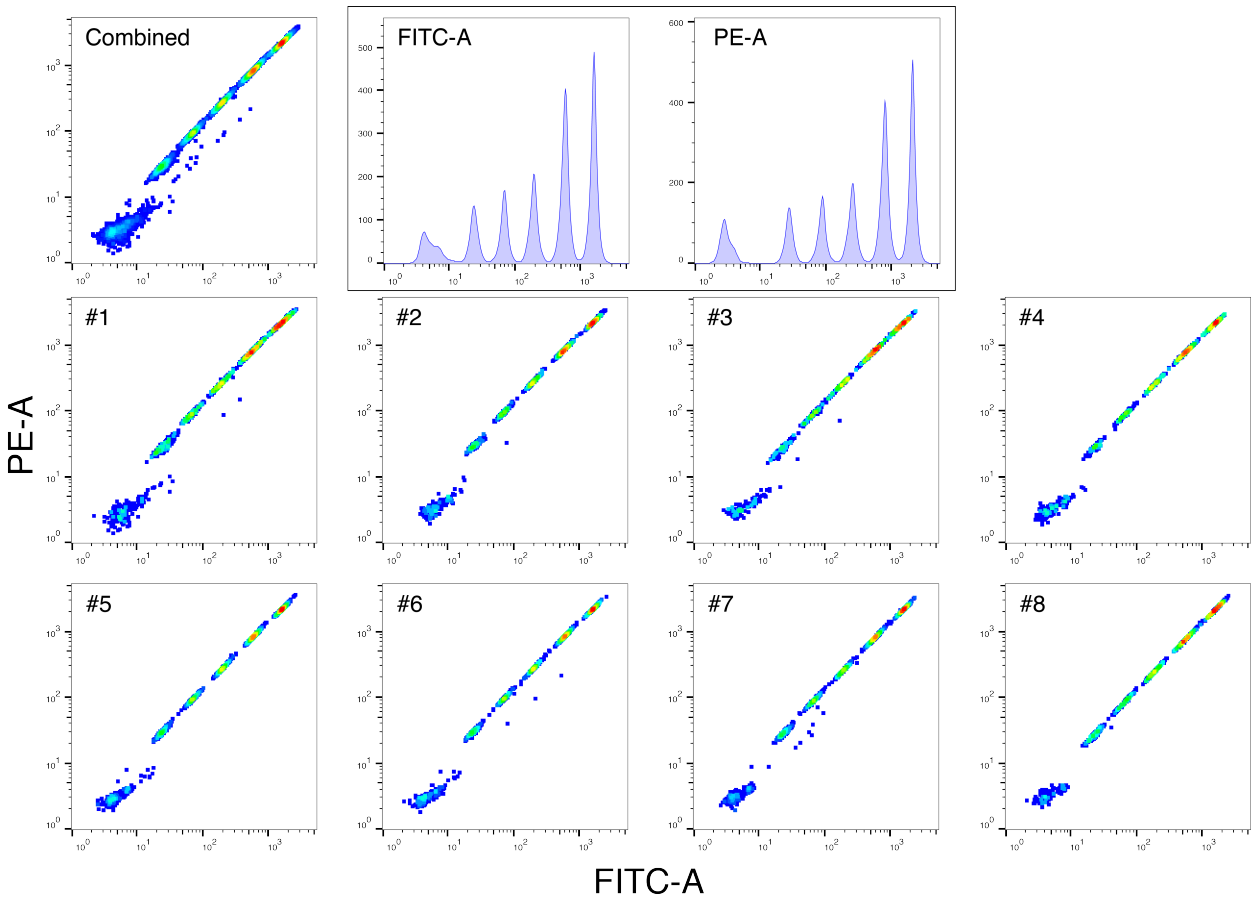

Figure 3.4: 6-peak calibration beads in 8 sample streams.
Six peak calibration beads were infused into all 8 sample inlets. After detection of sample stream of origin for each event and application of a multiplicative equalization factor to each channel, all 6 peaks are visible in both FITC and PE channels for all 8 sample streams. The upper left plot shows combined FITC and PE data from all 8 channels. Histograms show separation of the 6 peak beads in the combined data. The eight scatter plots in the bottom two thirds show each of the 8 sample streams. 6 bead populations are visible in all eight streams.

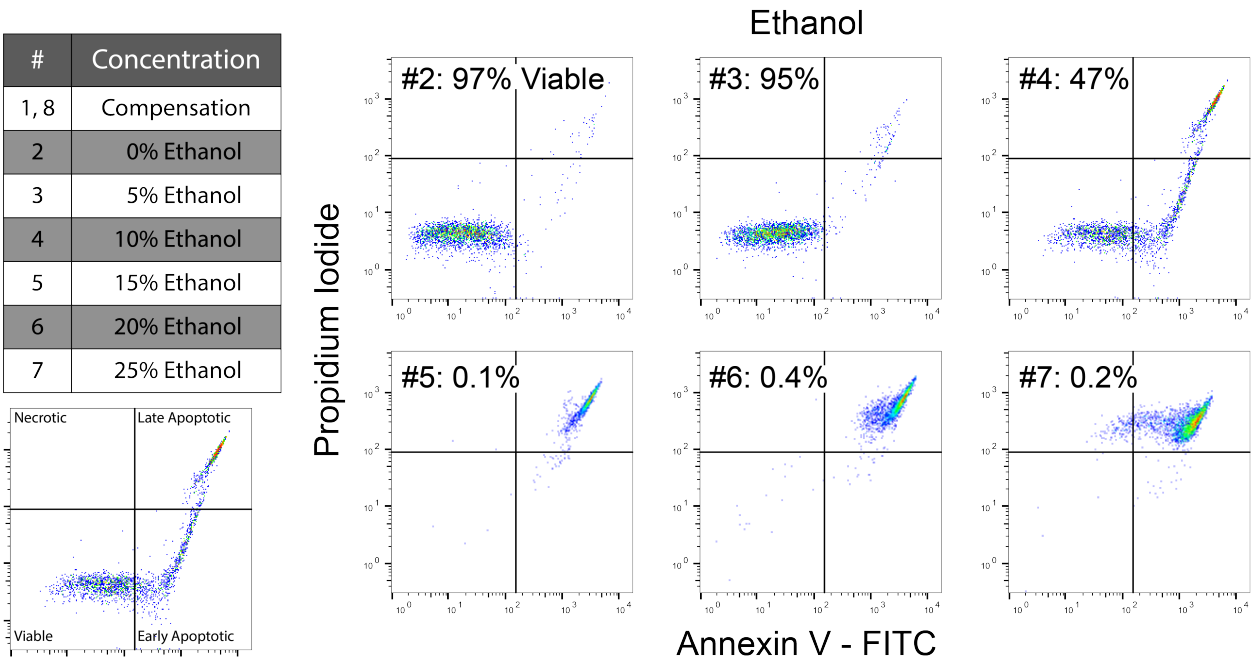

#	Concentration
1, 8	Compensation
2	0% Ethanol
3	5% Ethanol
4	10% Ethanol
5	15% Ethanol
6	20% Ethanol
7	25% Ethanol

Figure 3.5: Half maximal inhibitory concentration (IC_{50}) experiment.
Jurkat cells were treated with varying concentrations of ethanol for one hour. The cells were then labeled with Annexin V, a marker of early apoptosis, and with propidium iodide (PI), a cell membrane impermeable nucleic acid stain that serves as an indicator of cell death. *Upper left*: Legend of treatment conditions. Samples 1 and 8 were designed as experiments to compensate for spectral overlap of FITC and PI. *Lower left*: Gating strategy. Cells that are FITC and PI negative (FITC-/PI-) are considered viable. Cells that are FITC+/PI-, FITC+/PI+, or FITC-/PI+ are considered early apoptotic, late apoptotic, or necrotic, respectively. *Right*: Results from 6-point IC_{50} experiment. Increasing concentrations of ethanol is correlated with increasing degrees of apoptosis. It is important to note that all 6 samples and 2 compensation experiments were measured simultaneously at a total volumetric sample throughput of 960 microliters per minute.

#	Camptothecin
1, 8	Compensation
2	0 μM
3	0.01 μM
4	0.1 μM
5	1 μM
6	10 μM
7	100 μM

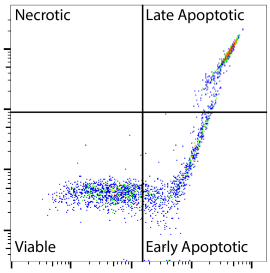

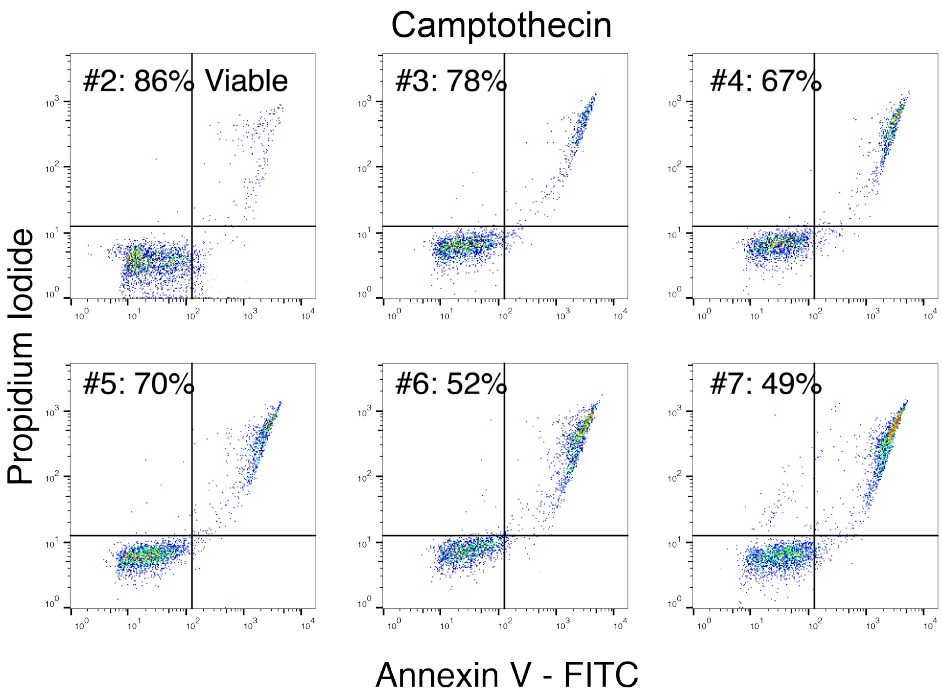

Figure 3.6: Half maximal inhibitory concentration (IC_{50}) experiment.
Jurkat cells were treated with varying concentrations of camptothecin for 24 hours. The cells were then labeled with Annexin V, a marker of early apoptosis, and with propidium iodide (PI), a cell membrane impermeable nucleic acid stain that serves as an indicator of cell death. *Upper left*: Legend of treatment conditions. Samples 1 and 8 were designed as experiments to compensate for spectral overlap of FITC and PI. *Lower left*: Gating strategy. Cells that are FITC and PI negative (FITC-/PI-) are considered viable. Cells that are FITC+/PI-, FITC+/PI+, or FITC-/PI+ are considered early apoptotic, late apoptotic, or necrotic, respectively. *Right*: Results from 6-point IC_{50} experiment. Increasing concentrations of camptothecin is correlated with increasing degrees of apoptosis. It is important to note that all 6 samples and 2 compensation experiments were measured simultaneously at a total volumetric sample throughput of 960 microliters per minute.

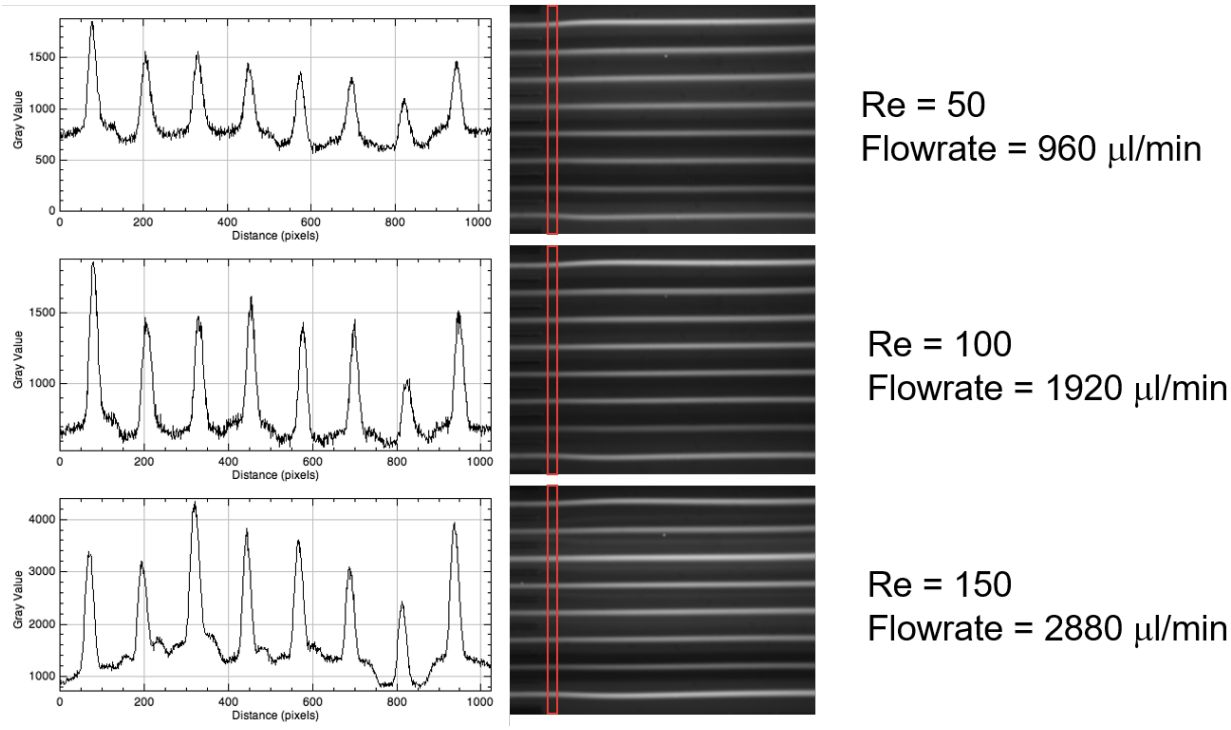

Figure 3.7: Fluorescent streak images of the flow cell interrogation region. Jurkat cells stained with Calcein Red-Orange were infused at a wide range of flowrates into the HIDRA flow cell. At Reynolds number = 50, cells are focused to the midlines of the flow focusing channels and particle inertia maintains spacing between sample streams in the interrogation region. This effect holds for Re 100 and 150 as well. Line traces of the interrogation region show a single fluorescent peak per sample stream, indicating effective spatial focusing. The appearance of elevated "shoulders" near some line trace peaks for the Re = 150 sample indicates degradation of performance likely due to develop of equilibrium positions along the lateral walls of the channels due to high Re.

Numerous papers in the past have claimed to achieve parallel cytometry without fully integrated systems or with optical systems that lack the speed and sensitivity of traditional flow cytometer hardwares. Our system represents a true parallel cytometer capable of performing multiparameter, single cell measurements at throughputs compatible with the needs of applications such as drug screening.

There are numerous improvements that can be made to the system described here. The most obvious improvement that can be made is the incorporation of additional fluorescence detectors. Currently the system sports two fluorescence channels and can easily be extended to include two additional channels excited by the 488 nm laser (e.g. Texas Red and PE-Cy5). Further expansion of detection capabilities is substantially more difficult, requiring the integration of additional excitation lasers. This integration can be done by building additional AOD and interferometer systems, but this approach has a large geometric footprint. Alternatively, the additional lasers can be integrated into the existing AOD and interferometer system. This approach would be difficult to design and require careful alignment due to the fact that deflection angles produced by the AOD are wavelength dependent.

Another possible future direction for this project would be integration of an automated sampling system. Such a system would require the syringe pump system to be replaced with a pressure driven system. Both positive and negative (vacuum) pressure systems can potentially work but both have unique implementation challenges. Pressurizing a wellplate is difficult and can lead to air being forced into the microfluidic channels where it is difficult to purge. On the other hand, using a vacuum to drive flow can lead to cavitation. Also, it is unclear if a single atmosphere of pressure differential is adequate to achieve inertial focusing.

Yet another possible future direction is modification of the FIRE illumination scheme to allow for imaging cytometry of each of the sample streams. Instead of using a single amplitude modulated excitation spot for each fluid stream, an array of spots can be used instead. Collectively, the spots on a given fluid stream would function as a line scan camera with each spot acting as a single pixel. This approach would add tremendous amounts of data to the measurement, allowing for localization of scatter and fluorescence, enabling high

content analysis such as colocalization of fluorophores, measurements of particle size, and measurements of fluorescence distribution.[19–22] This approach requires substantially higher AOD frequency bandwidth because modulation frequencies of adjacent pixels need to sufficiently spaced in the frequency domain to prevent frequency spreading, caused by fast moving objects, from corrupting the image.

3.5 Acknowledgments

Keegan Owsley and Eric Diebold at Omega Biosystems assisted with the design and construction of optical, electronic, and signal processing systems used in these experiments.

3.6 References

[1] J P Hughes et al. "Principles of early drug discovery." In: *British journal of pharmacology* 162.6 (Mar. 2011), pp. 1239–49.

[2] Bruce S. Edwards and Larry A. Sklar. *Flow cytometry: Impact on early drug discovery.* July 2015.

[3] Christopher B. Black et al. "Cell-Based Screening Using High-Throughput Flow Cytometry". In: *ASSAY and Drug Development Technologies* 9.1 (2011), pp. 13–20.

[4] Robert A. Hoffman and James C.S. Wood. "Characterization of Flow Cytometer Instrument Sensitivity". In: *Current Protocols in Cytometry.* Vol. Chapter 1. Hoboken, NJ, USA: John Wiley & Sons, Inc., Apr. 2007, Unit1.20.

[5] David R. Parks et al. "Evaluating flow cytometer performance with weighted quadratic least squares analysis of LED and multi-level bead data". In: *Cytometry Part A* 91.3 (2017), pp. 232–249.

[6] Aram J. Chung, Daniel R. Gossett, and Dino Di Carlo. "Three Dimensional, Sheathless, and High-Throughput Microparticle Inertial Focusing Through Geometry-Induced Secondary Flows". In: *Small* 9.5 (Mar. 2013), pp. 685–690.

[7] Daniel R. Gossett and Dino Di Carlo. "Particle Focusing Mechanisms in Curving Confined Flows". In: *Analytical Chemistry* 81.20 (Oct. 2009), pp. 8459–8465.

[8] John Oakey et al. "Particle focusing in staged inertial microfluidic devices for flow cytometry". In: *Analytical Chemistry* 82.9 (2010), pp. 3862–3867.

[9] Gregory Goddard et al. "Ultrasonic particle-concentration for sheathless focusing of particles for analysis in a flow cytometer". In: *Cytometry Part A* 69A.2 (Feb. 2006), pp. 66–74.

[10] Soojung Claire Hur, Henry Tat Kwong Tse, and Dino Di Carlo. "Sheathless inertial cell ordering for extreme throughput flow cytometry." In: *Lab on a chip* 10.3 (2010), pp. 274–280.

[11] Brian K. McKenna et al. "A parallel microfluidic flow cytometer for high-content screening". In: *Nature Methods* 8.5 (May 2011), pp. 401–403.

[12] Menake E. Piyasena et al. "Multinode acoustic focusing for parallel flow cytometry". In: *Analytical Chemistry* 84.4 (Feb. 2012), pp. 1831–1839. arXiv: `NIHMS150003`.

[13] Y. J. Fan et al. "Three dimensional microfluidics with embedded microball lenses for parallel and high throughput multicolor fluorescence detection". In: *Biomicrofluidics* 7.4 (July 2013), p. 044121.

[14] Eric D. Diebold et al. "Digitally synthesized beat frequency multiplexing for sub-millisecond fluorescence microscopy". In: *Nature Photonics* 7.10 (2013), pp. 806–810.

[15] D. R. Gossett et al. "Hydrodynamic stretching of single cells for large population mechanical phenotyping". In: *Proceedings of the National Academy of Sciences* 109.20 (May 2012), pp. 7630–7635.

[16] Henry T K Tse et al. "Quantitative diagnosis of malignant pleural effusions by single-cell mechanophenotyping." In: *Science translational medicine* 5.212 (Nov. 2013), 212ra163.

[17] Hamed Amini, Wonhee Lee, and Dino Di Carlo. "Inertial microfluidic physics". In: *Lab on a Chip* 14.15 (July 2014), p. 2739.

[18] Jonathan Lin et al. “High-throughput physical phenotyping of cell differentiation”. In: *Microsystems & Nanoengineering* 3.December 2016 (2017), p. 17013.

[19] Nao Nitta et al. “Intelligent Image-Activated Cell Sorting.” In: *Cell* 0.0 (Aug. 2018).

[20] Hideharu Mikami et al. “Ultrafast confocal fluorescence microscopy beyond the fluorescence lifetime limit”. In: *Optica* 5.2 (Feb. 2018), p. 117.

[21] Sadao Ota et al. “Ghost cytometry.” In: *Science (New York, N.Y.)* 360.6394 (June 2018), pp. 1246–1251.

[22] Thomas Blasi et al. “Label-free cell cycle analysis for high-throughput imaging flow cytometry”. In: *Nature Communications* 7 (Jan. 2016), p. 10256.

CHAPTER 4

Integrated Deformability and Fluorescence Imaging Cytometry

Jonathan Lin, Lillian Peng, Bonnie Yeh, Tridib Biswas, Dino Di Carlo

In recent years, biophysical phenotyping has emerged as a promising method of assaying cell states including differentiation, neoplasia, and immune activation. Thus far, mechanical phenotyping and traditional biochemical labeling at the single-cell level have only been studied separately or at extremely low throughputs. In this chapter, we demonstrate a microfluidic device that performs high-throughput, continuous, single-cell measurements of both mechanical and biochemical phenotype. To accomplish this, we integrate an ultra-high-speed fluorescent imaging system with a microfluidic device featuring a tunable constriction to perform biochemical profiling as well as measurements of the deformation of subcellular compartments. By performing measurements in a high-throughput, single-cell manner, we establish one-to-one correlations of biochemical markers and physical properties with sample sizes representative of the entire population. In doing so, we open the door to a deeper understanding of the molecular factors that contribute to the physical properties of cells and add an entirely new dimension, physical phenotype, to traditional biochemical cytometry.

4.1 Introduction

Recent years have born witness to a growing interest in cell mechanical properties as integrated measurements of cell state.[1–11] Mechanical properties have been used as label-free methods of assaying cell differentiation, immune activation, and neoplastic processes. Previ-

ous work has shown that mechanical properties are predictive of the differentiation potential of stem cells and that stem cells can be distinguished from differentiated cells via their mechanical properties.[6,7] Additionally, others have shown that mechanical properties have diagnostic value and have been used to identify inflammation and neoplasia in pleural effusions.[3,4]

There currently exist several techniques to measure cell mechanical properties. Techniques such as micropipette aspiration, optical tweezers, and atomic force microscopy (AFM) have existed for a while but are inherently low throughput, making it difficult to perform measurements on large numbers of cells. In recent years, novel, high-throughput methods have been developed using extensional flows to stretch cells and narrow channels to apply shear forces.[1–6]

While mechanophenotyping cells is relatively new, biochemical phenotyping of cells through techniques such as immunolabeling has a long and rich history. Techniques such as fluorescence microscopy and flow cytometry have existed for decades and are technologically mature. There is a massive body of literature demonstrating the power of these techniques and a large portion of our understanding of biology is based on measurements performed on these instruments.

Thus far, however, researchers have been unable to bridge the divide between mechanophenotyping technologies and traditional fluorescence-based measurements of biomolecular markers. Techniques capable of mechanical and fluorescence measurements such as confocal AFMs are expensive and low-throughput, making it difficult to achieve statistical power and to detect subpopulations of cells. Yet, these technologies are used, indicating the need for an instrument capable of high-throughput mechanical and fluorescence measurements.[12]

The difficulty associated with correlating mechanical properties and biomolecular markers at a single cell level has hindered the study of the molecular underpinnings of cell physical phenotypes. It has also prevented the mechanophenotyping of cellular subpopulations. Additionally, the inability to perform fluorescence imaging in conjunction with mechanical measurements has also prevented the study of subcellular compartments such as cell nuclei

and their contributions to cell mechanical properties.

In this chapter, we present a fluorescence imaging deformability cytometer (F-DC) that combines two technological innovations (i) tunable hydrodynamic stretching of cells under the influence of viscous sheathing streams and (ii) line-scan in-flow fluorescence imaging using radiofrequency-tagged emission (FIRE) that enables fluorescence imaging of deforming cells at throughputs exceeding 100 cells per second. It combines the multiparameter molecular detail enabled by fluorescence in standard flow cytometers with additional morphological and mechanical properties typically captured using high speed cameras.

We show that this system is capable of measuring the deformability of hundreds of cells per second with single cell level correlation with up to four fluorescent markers. We demonstrate this capability by treating cells with drugs that modulate the cytoskeleton and observing the corresponding changes to cellular deformability. Additionally, we perform fluorescence sensitivity testing using standard 6-peak fluorescent calibration beads.

We also show that the system is capable of subcellular imaging, allowing us to study the deformation of the nucleus and the effect of the nucleus on cell mechanical properties. We demonstrate this capability by osmotically shocking cells with a hypo-osmotic solution prior to measurement of nuclear deformation and whole cell deformability. This biological test system was chosen because it has been previously shown that osmotic stress can induce structural changes to cell nuclei which can result in changes in gene expression.[13–15]

Finally, we show that the system is capable of detecting cellular subpopulations based on mechanical properties or fluorescent labels, enabling detailed study of subpopulations that has not previously been possible. We use this capability to perform deformability measurements at various points in the cell cycle using cells transfected with the FUCCI plasmid. Previous studies of the mechanical changes that occur during the cell cycle have relied on artifically arresting the cell cycle in order to produce pure populations for measurement.[1] Our approach allows these measurements to be performed without the need for cell cycle synchronization which can alter the phenotype of cells.

4.2 Results and Discussion

4.2.1 Microfluidic Stretching of Cells With Viscous Sheath Flows

The microfluidic device used in F-DC has three functional regions. The inlet region contains three inlets, a sample inlet flanked on both sides by viscous sheath flow inlets. These channels converge in the flow focusing region where the viscous sheath flows act to focus cells to the channel midline. This allows for uniform delivery of cells to the next region, the deformation region. In this region, the channel narrows into a constriction where the sheath flow acts to accentuate the forces on cells, causing them to deform (Figure 4.1A, 4.1B). The accentuation of forces due to the viscous sheath flow allows for the channel cross-sectional area (30 x 25 μm) to be substantially larger than that of a cell. The importance of viscous sheathing is demonstrated in Figure 4.5 where the absence of a higher viscosity sheath flow leads to dramatically lower deformations. Both sheath flows are infused at 5 μl/min with the sample infused at 10 μl/min between them. This 1:1 ratio of sheath flow is selected such that the fluid lumen is approximately 5 microns in width (Figure 4.6). This narrow lumen ensures that cells, regardless of size, are uniformly in contact with the sheathing fluid. Higher sheath velocities would increase the shear forces on cells but the imaging system places an upper limit on cell velocity due to image degradation caused by fast moving objects.

F-DC is an improvement upon a previously described system where cells were resuspended in a viscous solution (0.5% w/v methylcellulose) and then flowed through a channel with approximately the same cross-sectional area as the cell. This system is prone to clogging and suspending cells in the viscous medium prior to measurement can lead to unintended changes in cell phenotype.[1,2]

4.2.2 Analysis of Cell Images and Imaging Performance

Imaging of deformed cells is performed using a Vulcan imaging system (Omega Biosystems). The system generates line of laser spots, each amplitude modulated at a unique frequency (Figure 4.1C). These lasers spots are imaged half way down the channel constriction such

that cells pass through the laser spots as they flow through the channel. Transmitted light, scattered light, and fluorescence emission are all tagged with the radiofrequency modulation and collected into single pixel detectors. Image reconstruction can then be performed using a sliding window FFT (Figure 4.1C). Image quality of both brightfield and FITC fluorescence images can be seen in Figure 4.1D. Pixel pitch is nominally 250 nm but adjacent pixels cannot be fully resolved due to the diffraction limit. Pixel height is determined by the size of the window used in the sliding window FFT in conjunction with the linear flow velocity. Fluorescence sensitivity was measured using 6-peak fluorescent beads (Figure 4.6). All six peaks are distinguishable in the FITC, PE, PE-Texas Red, and PE-Cy5 channels (Figure 4.6).

Extraction of whole cell and nuclear deformation is performed using automated computer analysis. Cells are imaged in brightfield and FITC after being treated with Syto16, a nucleic acid stain. The resulting images are thresholded and circularity is computed as a metric of deformation. Other metrics, including cell area and nuclear area, are computed as well. Example results from the cell detection are shown in Figure 4.7. The extraction of morphologic information takes approximately 3 ms per cell. Thus, the system can perform real time measurements of deformability up to an event rate of approximately 300 per second. This rate is sustainable as long as there is sufficient computer RAM. If images of cells are not retained, the rate can be sustained forever. The main bottleneck of the processing pipeline is the generation of cell images which currently utilizes a single-threaded sliding window FFT algorithm. Multithreading this algorith or replacing it with with GPU or FPGA accelerated code could substantially improve the maximum event rate. Alternatively, much higher event rates can be sustained if image reconstruction and processing is done after the data collection has ended.

4.2.3 Cytoskeletal Modulators

In order to assess the sensitivity of the F-DC system to cytoskeletal changes, HL-60 cells were treated with a variety of compounds with known effects on the cytoskeleton.

First, HL-60 cells were treated with 0.1 μM Cytochalasin D (CytoD). The resultant cells had a deformability of 1.13 relative to the vehicle control (DMSO). This result matches our understanding of the molecular mechanism of Cytochalasin D which inhibits actin polymerization, destabilizing the structure of the cell.[2]

Next, HL-60 cells were treated with 0.1 μM and 100 μM concentrations of nocodazole. The resultant cells showed a dose dependent change in deformability. Cells treated with 0.1 μM nocodazole had a deformability of 1.12 relative to the vehicle control (DMSO). This matches our understanding of the molecular mechanism of nocodazole which inhibits the polymerization of microtubules, a structural component of cells.[2]

These experiments represent a proof of concept for the F-DC system, demonstrating that it is capable of observing the effects of cytoskeletal modulation.

4.2.4 Osmotic Swelling and the Nucleus

HL-60 cells were resuspended in PBS diluted to 270 mOsm/kg and 240 mOsm/kg with distilled water. Cells in the control group were resuspended in 1x PBS (300 mOsm/kg). After a short incubation time, the cells were stained with Syto 16.

The resultant cells showed no clear trend in whole cell deformability (Figure 4.3). Relative deformability decreased slightly to 0.94 for cells exposed to 270 mOsm/kg. However, relative deformability increased to slightly to 1.04 for cells exposed to 240 mOsm/kg. Cell size showed a similar trend with cell area decreasing from 1765 px^2 to 1693 px^2 from the control group to the 270 mOsm/kg group. Cells treated with 240 mOsm/kg solution had cell sizes larger than control at 1896 px^2.

Although there was no clear trend in whole cell deformability, there was a dose dependent effect on nuclear size and deformation. Treatment with 270 mOsm/kg solution corresponded with an increase in relative deformation to 1.03. Treatment with 240 mOsm/kg solution corresponded with further increase in deformation to 1.07. It is worth noting that the F-DC system does not decouple the deformation of the nucleus from the deformation of the

entire cell. Thus, the measured nuclear deformation is the result of whole cell and nuclear mechanical properties. There was a similar trend in nuclear size as well. The control group had median nuclear area of 864 px^2 while the 270 mOsm/kg and 240 mOsm/kg treatment groups had nuclear areas of 878 px^2 and 919 px^2, respectively.

Nucleus to cytoplasm (N:C) ratio was investigated to determine the effect of the nucleus on the measured whole cell deformability. The 270 mOsm/kg sample showed an increase in N:C ratio from the control group's median N:C ratio of 0.495 to 0.519. The 240 mOsm/kg sample, on the other hand, showed a small decrease to 0.488. Interestingly, the increase in N:C ratio in the 270 mOsm/kg sample corresponded to a decrease in whole cell deformability to a relative deformability of 0.97. Similarly, the small decrease in N:C ratio in the 240 mOsm/kg sample corresponded to an increase in deformability to a relative deformability of 1.02. The relationship between N:C ratio and whole cell deformability requires further study but there appears to be a negative correlation between the two parameters.

Overall, these experiments demonstrate that F-DC has the capability of studying subcellular compartments such as the nucleus and their contribution to the overall deformability of a cell. Further work needs to be done to understand the trends that we observed in the course of these experiments. It would be particularly interesting to examine the effects of hyperosmolar stress which has been shown to cause linear changes in cell and nuclear volume. Hypo-osmolar stress, on the other hand, has been shown to have a linear relationship with cell volume and a asymptotic relationship with nuclear volume. The osmolar stresses tested in the literature are greater in magnitude than what we have tested in our F-DC system. It is possible that expanding the osmolar range that we test would yield similar trends to what is reported in literature.[13]

4.2.5 Cell Cycle Effect on Deformability

A long-standing problem in cell mechanical measurements is the effect of cell cycle on mechanical properties. Previous work has been done to measure mechanical properties at different points in the cell cycle but these techniques have relied on low throughput mea-

surements or chemical synchronization of cells. Here, we attempt to study the mechanical changes associated with the cell cycle in a high-throughput fashion without the need for synchronization that may alter cell phenotypes. To do this, we utilized K562 cells transfected with the FUCCI plasmid. This plasmid expresses GFP-geminin and RFP-cdt1. Geminin is degraded during the G1 phase of the cell cycle and Cdt1 is degraded during the S, G2, and M phases. Thus, transfected cells will fluoresce green during S, G2 and M phases and will fluoresce red during G1. During the transitions between G1 and S, transfected cells will become double positive for GFP and RFP.[16]

Transfected cells were infused into the F-DC system and their cell area and deformability were measured. The gating strategy that we employed is shown in Figure 4.4. GFP+/RFP- cells were found to be on average larger (2501 px^2) and more deformable (0.133) than cells in other parts of the cell cycle. GFP+/RFP+ cells (area = 2267 px^2, deformability = 0.121) were very similar to RFP+ cells (area = 2283 px^2, deformability = 0.119) both in size and deformability. These trends appear to match previously reported trends with cells becoming larger and more deformable during the leadup to mitosis.[1]

4.3 Materials and Methods

4.3.1 Chip Design and Manufacture

The microfluidic flow cell was manufactured using traditional soft lithography techniques. Features were transferred to wafers spin-coated with a 30 μm layer KMPR 1025 (Microchem) to produce a mold. Silicone elastomer (Sylgard 184, Dow Corning) was molded off the wafers and then bonded to glass using a reactive ion etcher (Technics). Fluidic interfacing was done using PEEK tubing (IDEX) and syringe pumps (Harvard Apparatus). Sheath flow is introduced at a total volumetric flow of 10 μl/min (5 μl/min on each side of the sample flow) and sample is introduced at a rate of 10 μl/min.

The device features two inlets, one for cell suspensions and another for a viscous sheathing fluid (1% w/v alginate in distilled water). The sheath flow acts to center cells prior to the

channel constriction where cells are deformed (Figure 4.1A). The gradual constriction leading up to the narrow channel acts to accelerate cells, increasing the spacing between cells and reducing the likelihood of doublet events and clogging (Figure 4.1B). The narrow channel where deformation occurs has a small cross sectional area (25 μm x 30 μm), causing cells to experience high shear forces. These forces are accentuated by the viscous sheath fluid which also acts to keep cells centered in the channel and away from the channel walls.

4.3.2 Optical System

A Vulcan imaging system (Omega Biosystems) was used to perform imaging. The system functions by passing a long coherence length, 100 mW, 488 nm laser through an acousto-optic deflector (AOD) which outputs 101 spatitally separated, frequency shifted beams of light. The frequency shifts are controlled by the signal passed into the AOD using an arbitrary waveform generator (Wavepond). The input signal is designed such that frequency shifts are uniformly spaced in the frequency domain. The first of the 101 beams is then picked off and reshaped using a flat top beam shaper. This local oscillator beam (LO) is interfered with the remaining 100 imaging beams in an interferometer. This results in a linear array of laser spots, each amplitude modulated at a frequency equal to the difference between the imaging beam frequency and the LO frequency. Thus, the spatial information of each 'pixel' is radiofrequency-encoded. It is important to note that the generation of this array of spots is entirely digitally controlled such that the amplitude modulation, maximum amplitude, and spatial location can be easily changed.

This array of laser spots is placed halfway along the narrow channel such that cells are fully deformed prior to passing through the imaging beam (Figure 4.1A). The transmitted light, scattered light, and fluorescence emissions, all of which are radiofrequency tagged, are then collected using single pixel detectors such as photomultiplier tubes (PMTs) and photodiodes. The resultant signals are traditional flow cytometry pulses combined with the radiofrequency-tagged spatial information (Figure 4.1C). Thus, a sliding window FFT can be utilized to recover the spatial information and render brightfield, darkfield, and fluorescent

images.

4.3.3 Image Analysis and Morphology Extraction

Measurements of cell size and deformability are done using a custom plugin designed for the Metis software (Omega Biosystems). Brightfield and fluorescence images are generated using the Metis software and then passed to the F-DC plugin. For brightfield images, a Otsu thresholding step is performed to isolate the cell membrane. Then hole-filling and removal of small objects is performed to create a solid cell mask. In cases where hole-filling is unsuccessful, a convex hull is fitted to the binary image. Next various morphology parameters, including cell area, are extracted using the open source scikit-image Python library. From here, the cell circularity, a measure of deformation, is computed according to Equation 1.

Once the cell area and deformability are computed, Metis can be used for gating and data processing. Debris and doublet events are typically removed using gates based on axial light loss and side scatter. Further gating is done to remove instances where the morphology extraction fails. Finally, scatter plots of the remaining data can be plotted and summary statistics on each of the parameters can be generated.

Equation 1:

$$\text{Circularity} = 4\pi(\text{Area}) \;/\; (\text{Perimeter})^2$$

4.3.4 Cytoskeletal Drug Treatments

HL-60 cells were cultured in RPMI 1640 base medium (Thermo Fisher Scientific) supplemented with 5% FBS (Thermo Fisher Scientific) and 1% penicillin-streptomycin (Thermo Fisher Scientific). Cells were cultured at 37° C, 5% CO2.

Cytochalasin D experiments were performed by dissolving cytochalasin D (Sigma-Aldrich) in DMSO prior to addition to cells suspended in PBS. Cells were incubated with cytochalasin D for 10 minutes at 37° C. Final DMSO concentration in experiments was 0.2%. Prior to

measurements, Syto16 was added to the cell suspensions to stain cell nuclei. Cell suspensions were then infused into the F-DC system without washing. Due to the nuclear staining, the FITC channel was used for triggering. Measurements were taken for up to 10 minutes following the start of infusion.

Nocodazole experiments were performed by dissolving nocodazole (Sigma-Aldrich) in DMSO prior to treatment. Cells suspended in PBS were treated with varying concentrations of nocodazole for 30 minutes at 37° C. Final DMSO concentration in experiments was 0.5% Prior to measurements, Syto16 was added so that it could be used as a triggering signal. Cell suspensions were then infused into the F-DC system without washing. Measurements were taken for up to 10 minutes following the start of infusion.

4.3.5 Osmotic Swelling Experiments

Dilutions of PBS produced by adding distilled water to 1x PBS (Gibco). Cells were resuspended in PBS and added 1:1 to diluted PBS to produce a hypo-osmolar environment. Cells were then incubated for 5 minutes at room temperature. Prior to measurements cells were stained with Syto 16 which was then used as a triggering signal. Cells were then infused into the F-DC system and measurements were taken for up to 15 minutes following the start of infusion.

4.3.6 Cell Cycle Experiments

FUCCI-transfected K562 cells were supplied by Dr. Claire Hur. Measurements were performed on cells during the log growth phase. Prior to measurement they were stained with LDS 751, a membrane permeant nucleic acid stain. This PE-Cy5 signal was used to determine if objects were nucleated cells or debris. Triggering was done with side scatter. Gating was performed on FITC and PE channels to select for GFP+/RFP-, GFP-/RFP+, and GFP+/RFP+ cells.

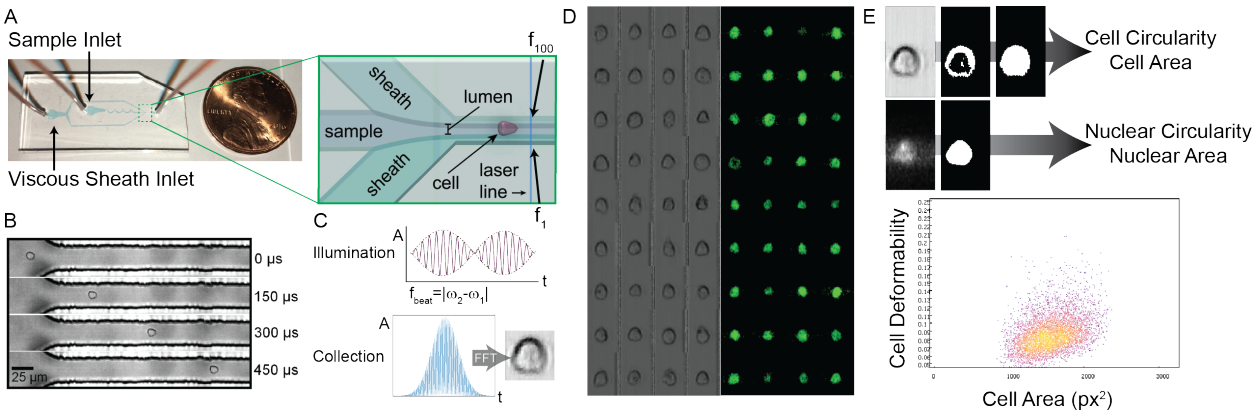

Figure 4.1: System schematic.
A) Fluidic and optical system design. Cell suspensions are introduced into a microfluidic chip with two inlets and a single outlet. Cells are centered and deformed in a narrow (25 μm) channel using a viscous sheathing flow. The deformed shape of the cell is captured using an ultra-high-speed fluorescent imager. B) Bright field images of cells deforming into "bullet-like" shapes in the narrow channel with viscous sheath flow. C) Ultra-fast fluorescent imaging is achieved by modulating the amplitude of the excitation laser (488 nm) such that each pixel along the laser line is modulated at a unique frequency. This modulation is achieved by interfering frequency-shifted beams to generate beat-frequency amplitude modulation. Fluorescent emission as well as scattered light are collected using PMTs. The collected waveforms are converted to images using a sliding window fast Fourier transform. D) Sample brightfield and fluorescent images generated by the system. Images are of HL-60 cells stained with Syto16, a membrane permeable nucleic acid stain. E) Automated analysis pipeline. Brightfield images are thresholded using the Otsu method to generate a Boolean image which is then converted to a solid region. Parameters such as cell circularity and area are then extracted. Similarly, fluorescent images of stained cell nuclei are thresholded and converted to solid regions from which parameters can be extracted. Both fluorescent and brightfield images can be acquired simultaneously, allowing measurements of cytoplasmic and nuclear properties simultaneously. The output of the analysis is single-cell-level mechanical and biochemical measurements, allowing for both subcellular mechanical measurements and correlation between mechanical properties and biochemical markers.

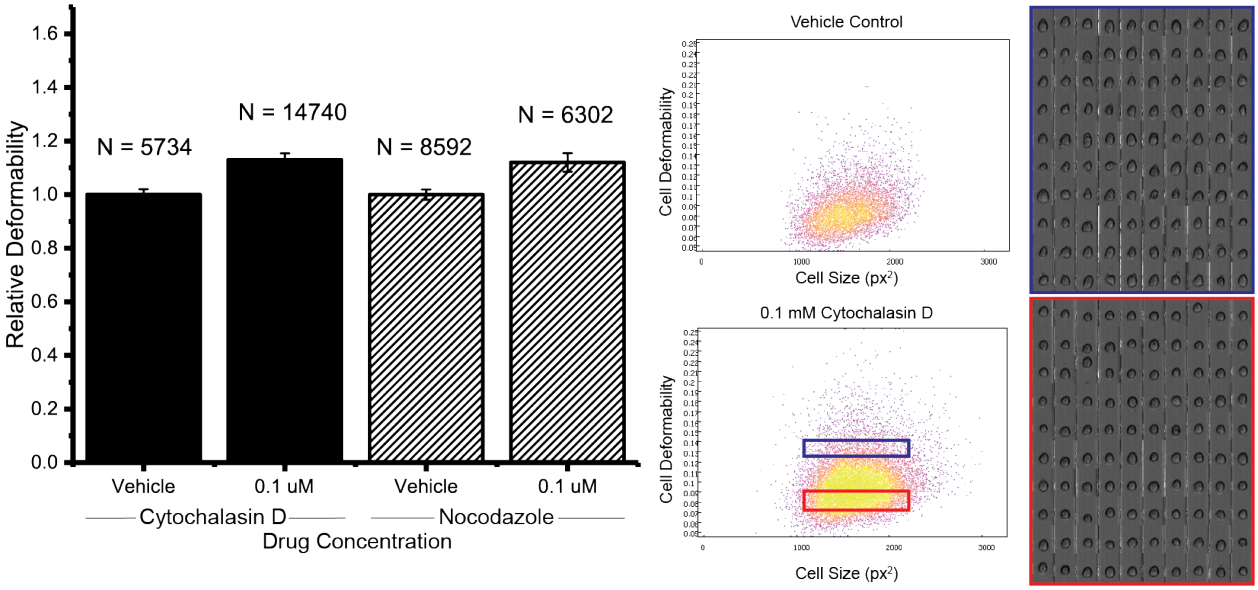

Figure 4.2: Cytoskeletal drug treatments.
HL60 cells were treated with varying concentrations of cytoskeletal drugs targeting actin and microtubules. Barplot: Both Cytochalasin D and Nocodazole, inhibitors of actin and microtubule polymerization, respectively, led to increases in relative deformability of cells. Bars represent median deformability and error bars represent one standard deviation. Scatter plots: Plots of cell area vs. cell deformability for single cell data show the change in deformability due to Cytochalasin D treatment. Image panels: Example images from each of the two populations present in HL60s treated with Cytochalasin D. The upper panel features cells that are more deformable while the lower panel depicts cells that are less deformable.

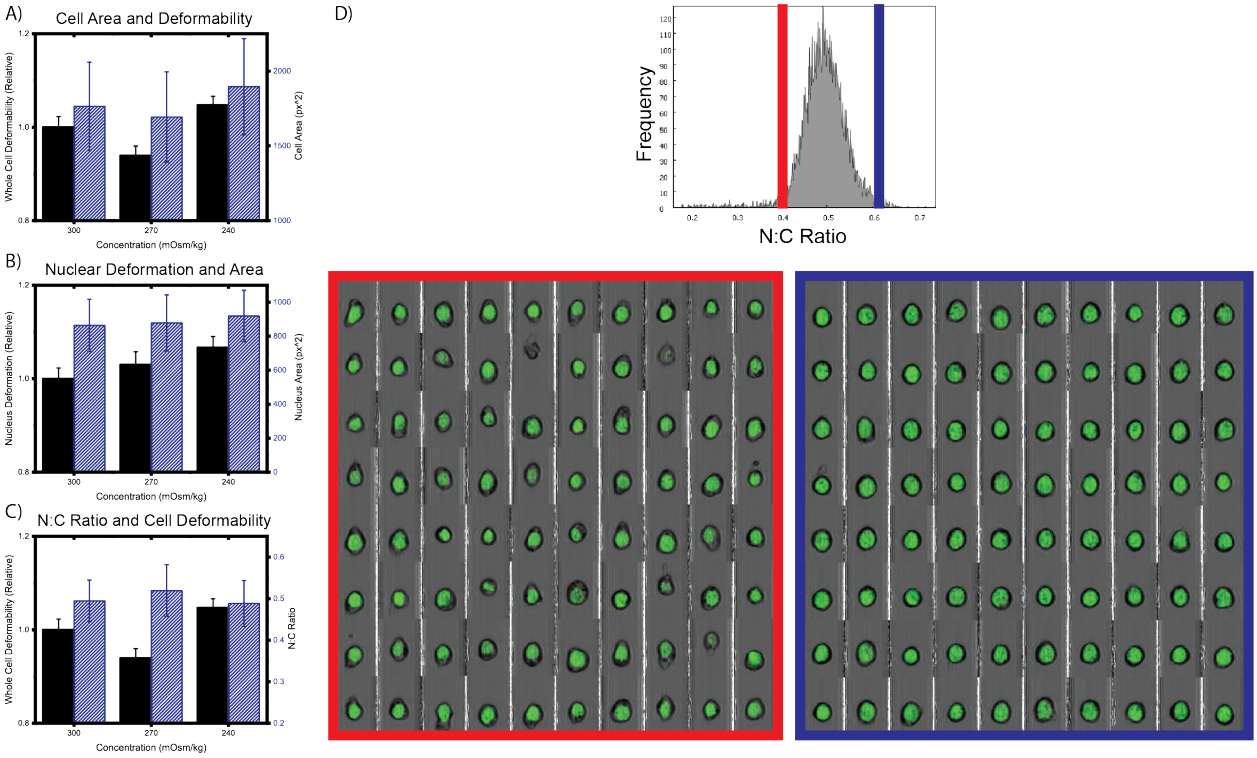

Figure 4.3: Osmotic swelling and nuclear Effects.
HL60 cells were exposed to an iso-osmolar environment (300 mOsm/kg) and varying degrees of hypo-osmolarity. A) Mild hypo-osmolar stress (270 mOsm/kg) results in cells that are smaller and with lower relative deformability while high hypo-osmolar (240 mOsm/kg) stress results in cells that are larger with higher relative deformability. B) Increasing levels of hypo-osmolar stress result in cell nuclei that are larger with higher relative deformation. C) Mild hypo-osmolar stress results in cells that have lower relative deformability but have a higher nucleus to cytoplasm (N:C) ratio. High hypo-osmolar stress results in cells that are more deformable with a lower N:C ratio. D) Example images of cells with an N:C ratio of approximately 0.4 (red) and 0.6 (blue).

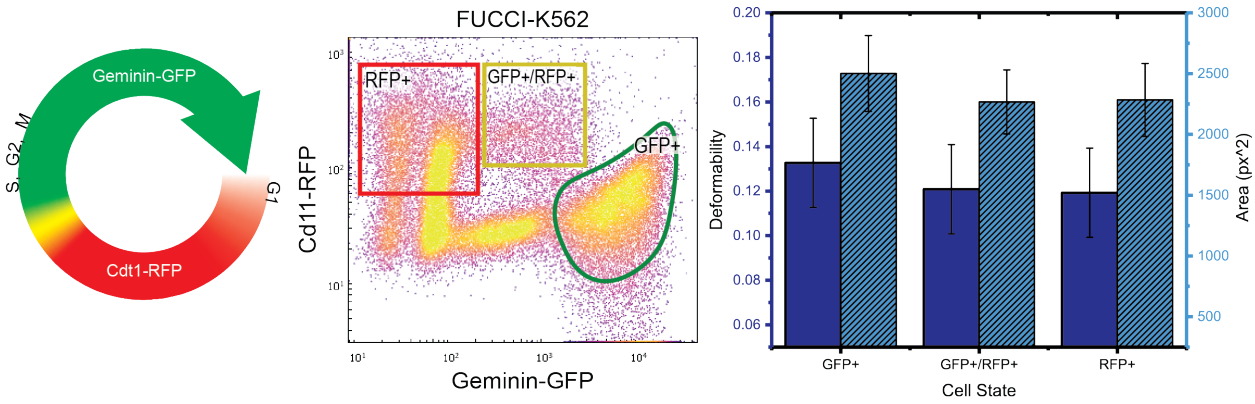

Figure 4.4: Cell cycle effects on deformability.
FUCCI-transfected K562 cells were measured using F-DC. Left: The FUCCI plasmid causes expression of geminin-GFP and Cdt1-RFP such that cells fluoresce green during S, G2, and M phases of the cell cycle and red during the G1 phase. During the brief transition between G1 and S, cells will express both GFP and RFP. Center: Gating strategy for identifying cell cycle stages. Right: Cells in S, G2, and M phases were found to be larger and more deformable than their counterparts. Cells in G1 and between G1 and S were similar in size and deformability.

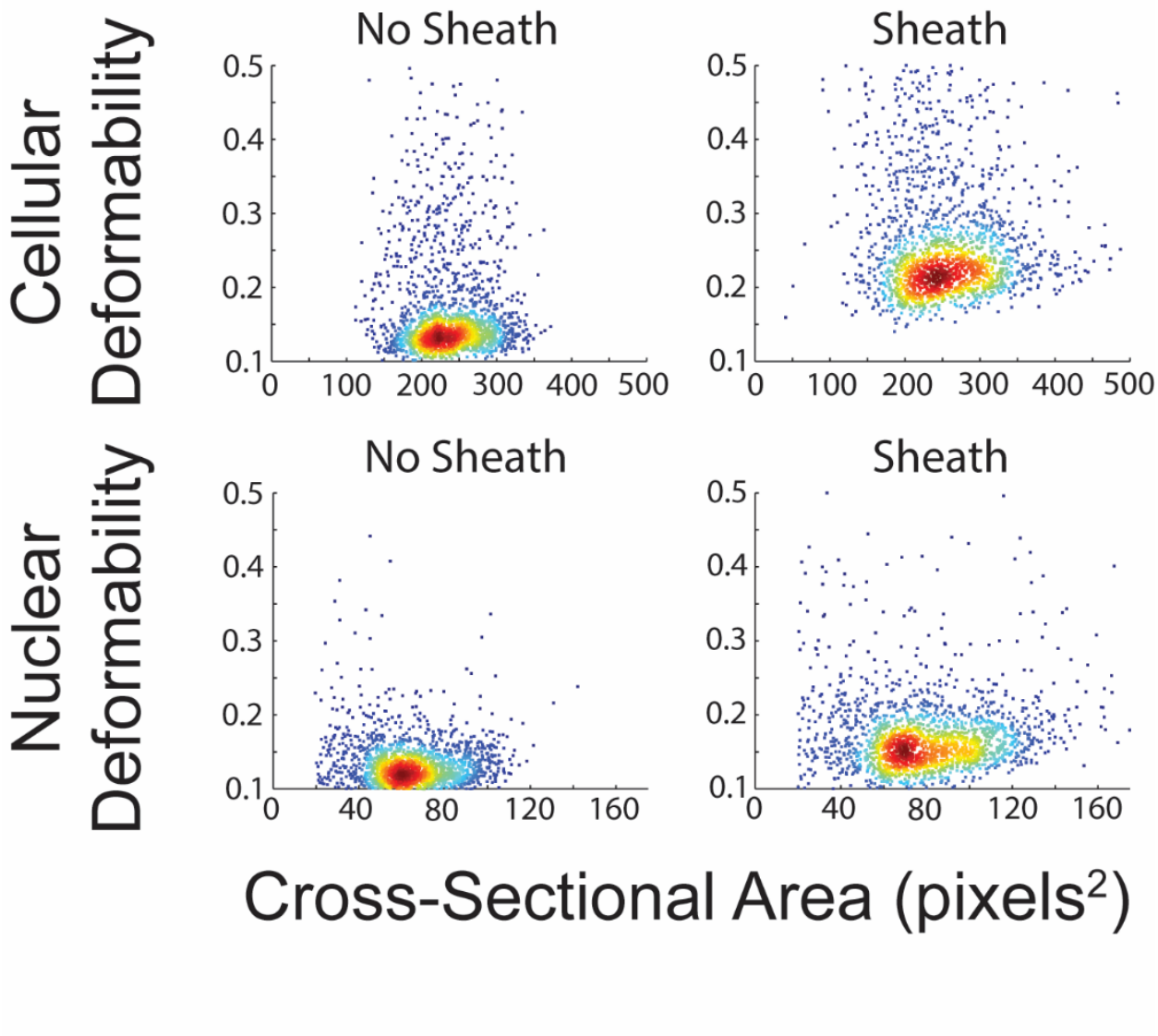

Figure 4.5: Effect of viscous sheath on cell deformation.
The F-DC system was run with either viscous sheath fluid (1% w/v alginate in water) or PBS as the sheath fluid. Use of viscous sheath increased the measured deformability of cells while use of PBS resulted in cells barely deforming. A similar effect is seen in nuclear deformation but is less pronounced.

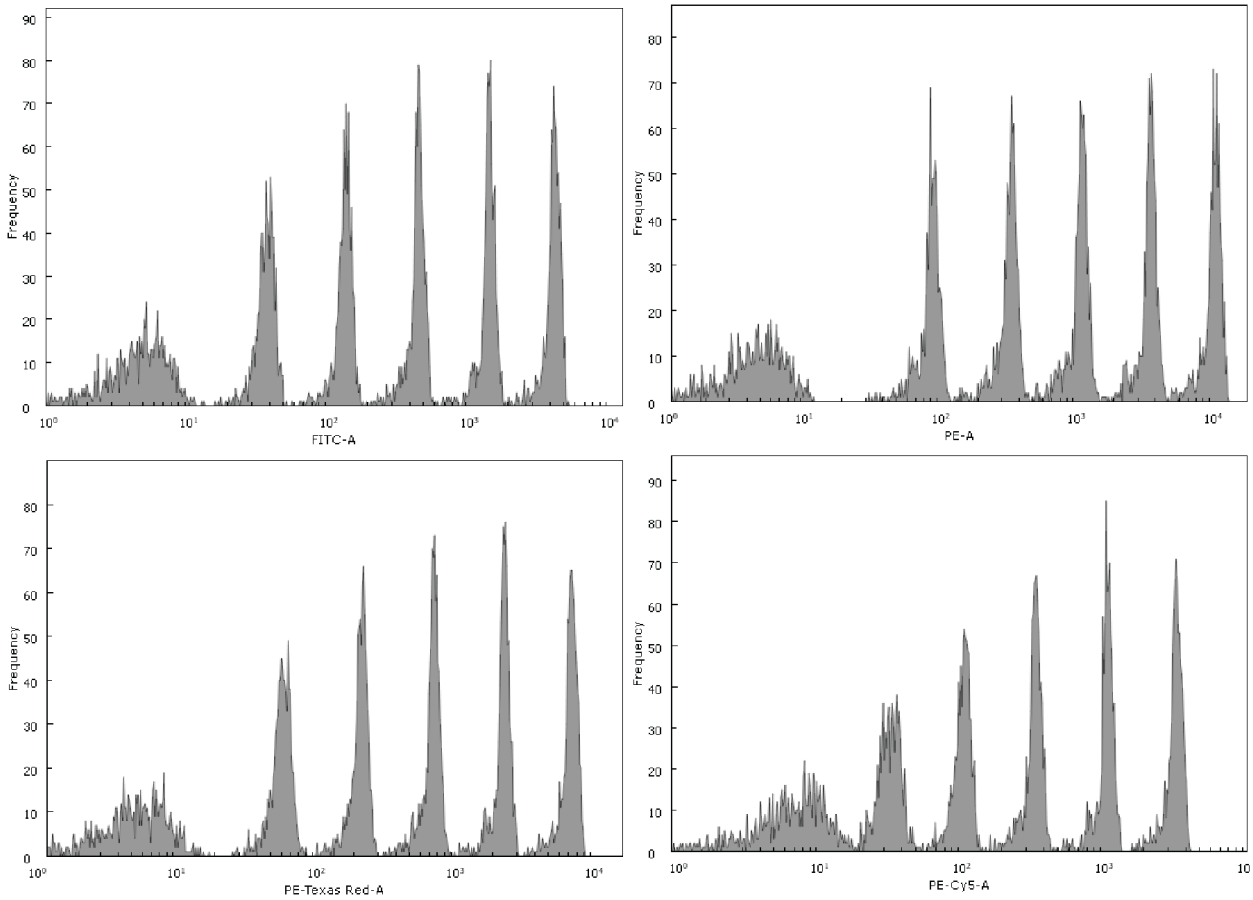

Figure 4.6: Fluorescence sensitivity of Vulcan imaging system.
6 peak fluorescent beads were used to measure the sensitivity of the imaging system. All 6 peaks are resolved in each of the four fluorescent channels with the best performance occurring in the PE channel. FITC channel performance is likely affected by PDMS autofluorescence and PE-Cy5 performance is likely affected by diminished PMT sensitivity in the far-red range.

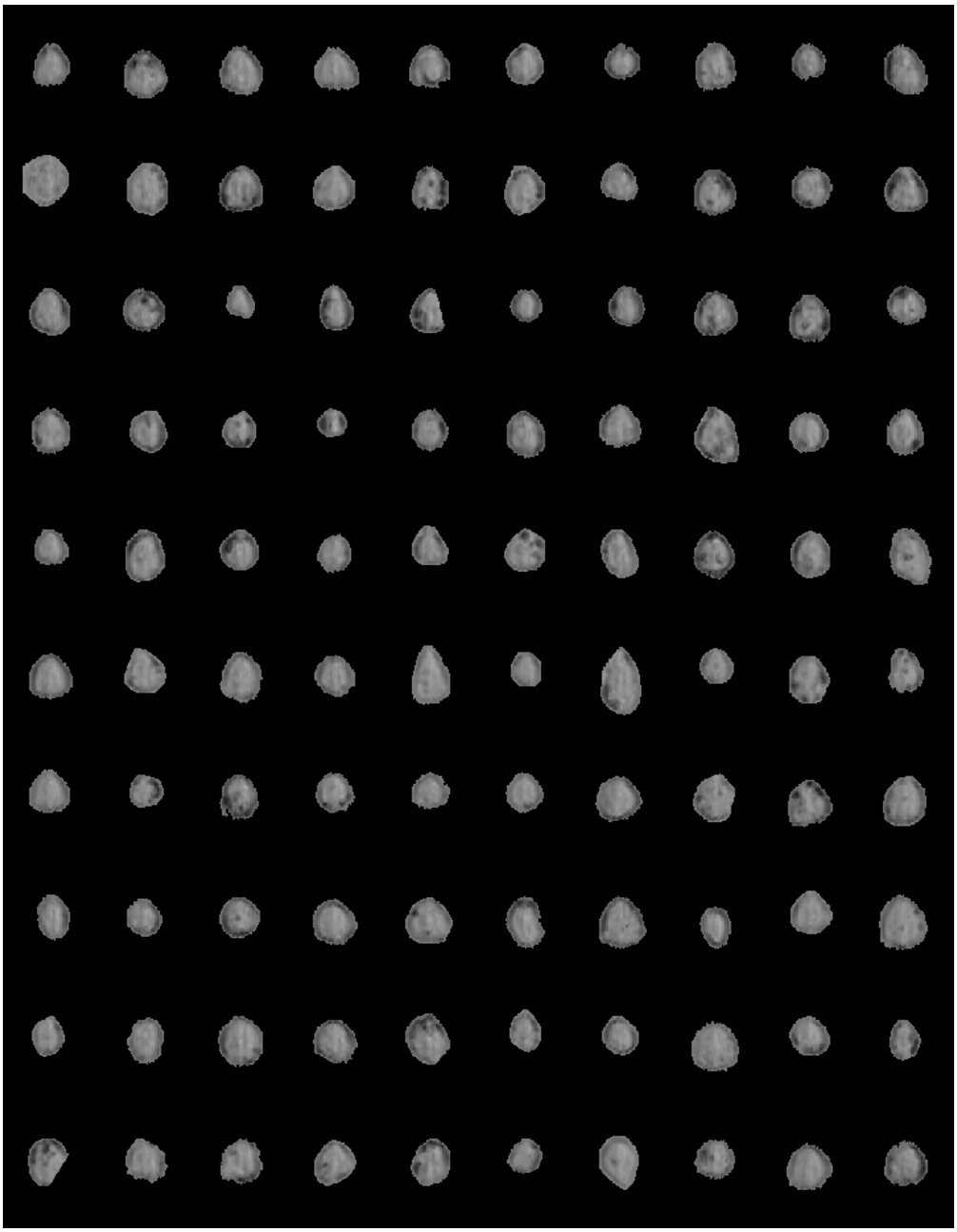

Figure 4.7: Example image of cell boundaries detected by the automated analysis algorithm. Membrane detection is performed by Otsu thresholding followed by hole filling or fitting of a convex hull. Cell morphology parameters including area and perimeter are extracted from the binary masks used to generate the above images.

4.4 Conclusions and Future Directions

In this chapter, we have demonstrated a new technique that combines traditional fluorescence cytometry with physical phenotyping. This technology enables high-throughput measurement of whole cell-deformability, subcellular deformations, and spatially-resolve fluorescence intensity. By establishing one to one correlations between biomarkers and mechanical properties on large populations of cells, this technology opens the door to understanding the molecular underpinnings of cell mechanical properties. Additionally, fluorescence imaging enables the study of subcellular compartments and their contribution to the physical phenotype of a cell. With the integration of fluorescence measurements, this technology finally connects the field of high-throughput physical phenotyping to the long-standing field of flow cytometry.

F-DC opens the door to understanding the role that mechanical properties play in complex biological systems. For instance, it can be used to study the mechanical changes that occur in subpopulations of leukocytes in response to immune stimuli. It can also be used to understand the mechanical changes that cancer cells undergo during metastasis. Furthermore, F-DC can be used to study the localization of cellular components to shed light on how cells control and regulate their mechanical phenotype.

From a technology development perspective, numerous improvements can be made to the F-DC system. Higher sample throughput can be achieved through a combination of a higher-bandwidth excitation system and parallelization of the image processing algorithms. Additionally, the sample and sheath infusion systems can be automated to test multiple shear stress conditions to develop more detailed mechanical profiles of populations of cells.

4.5 References

[1] Oliver Otto et al. “Real-time deformability cytometry: on-the-fly cell mechanical phenotyping”. In: *Nature Methods* 12.3 (2015).

[2] Stefan Golfier et al. “High-throughput cell mechanical phenotyping for label-free titration assays of cytoskeletal modifications.” In: *Cytoskeleton (Hoboken, N.J.)* 74.8 (Aug. 2017), pp. 283–296.

[3] D. R. Gossett et al. “Hydrodynamic stretching of single cells for large population mechanical phenotyping”. In: *Proceedings of the National Academy of Sciences* 109.20 (May 2012), pp. 7630–7635.

[4] Henry T K Tse et al. “Quantitative diagnosis of malignant pleural effusions by single-cell mechanophenotyping.” In: *Science translational medicine* 5.212 (Nov. 2013), 212ra163.

[5] Mahdokht Masaeli et al. “Multiparameter mechanical and morphometric screening of cells”. In: *Scientific Reports* 6.1 (Dec. 2016), p. 37863.

[6] Jonathan Lin et al. “High-throughput physical phenotyping of cell differentiation”. In: *Microsystems & Nanoengineering* 3.December 2016 (2017), p. 17013.

[7] R. D. Gonzalez-Cruz, V. C. Fonseca, and E. M. Darling. “Cellular mechanical properties reflect the differentiation potential of adipose-derived mesenchymal stem cells”. In: *Proceedings of the National Academy of Sciences* 109.24 (June 2012), E1523–E1529.

[8] Alexander Mietke et al. “Extracting Cell Stiffness from Real-Time Deformability Cytometry: Theory and Experiment”. In: *Biophysical Journal* 109.10 (Nov. 2015), pp. 2023–2036.

[9] Yanxiang Deng et al. “Inertial Microfluidic Cell Stretcher (iMCS): Fully Automated, High-Throughput, and Near Real-Time Cell Mechanotyping”. In: *Small* 13.28 (July 2017), p. 1700705.

[10] Marta Urbanska et al. “High-throughput single-cell mechanical phenotyping with real-time deformability cytometry”. In: *Methods in Cell Biology* 147 (Jan. 2018), pp. 175–198.

[11] Dongping Qi et al. “Screening cell mechanotype by parallel microfiltration”. In: *Scientific Reports* 5 (Dec. 2015), p. 17595.

[12] Timothy J Thauland et al. “Cytoskeletal adaptivity regulates T cell receptor signaling.” In: *Science signaling* 10.469 (Mar. 2017), eaah3737.

[13] John D Finan et al. “Nonlinear osmotic properties of the cell nucleus.” In: *Annals of biomedical engineering* 37.3 (Mar. 2009), pp. 477–91.

[14] John D Finan and Farshid Guilak. “The effects of osmotic stress on the structure and function of the cell nucleus.” In: *Journal of cellular biochemistry* 109.3 (Feb. 2010), pp. 460–7.

[15] Rui P Martins et al. “Mechanical regulation of nuclear structure and function.” In: *Annual review of biomedical engineering* 14 (2012), pp. 431–55.

[16] Asako Sakaue-Sawano et al. “Visualizing Spatiotemporal Dynamics of Multicellular Cell-Cycle Progression”. In: *Cell* 132.3 (Feb. 2008), pp. 487–498.

CHAPTER 5

Concluding Remarks

In the preceding chapters, we discussed three new technologies that represent improvements upon existing cytometry technologies. Multiparameter deformability cytometry adds new parameters that can be measured as part of a cell's mechanical phenotype. Parallel flow cytometry demonstrates true parallelization of flow cytometry measurements, achieving unprecedented sample throughputs. Fluorescence imaging deformability cytometry combines the power of fluorescent labeling with mechanophenotyping, enabling nuanced studies of the mechanophenotypes of heterogeneous cell populations and investigation of the underlying molecular origins of cell mechanical properties.

These technologies are parts of larger trends in cytometry towards high-throughput single-cell measurements with large degrees of multiplexing. Future technologies will likely continue down this path with instruments capable of mutiple categories of readouts including quantifying fluorescently labeled biomolecules, measuring mechanical properties, and sequencing of RNA and DNA.

Higher degrees of multiplexing will enable researchers to study complex biological systems with more nuance and will lead to the development of more comprehensive models of the cell and of cellular populations. These models will dramatically improve our understanding of disease and our ability to develop new therapeutics.

One major barrier to ever-increasing amounts of multiplexing is our ability to visualize and understand high-dimensional data. Techniques for data mining and data visualization have been evolving rapidly but are still in their infancy. There exist numerous transformations that have been developed to visualize high-dimensional data but they are often

non-parametric, new data cannot easily be projected to the transformed space, and non-deterministic, repeated transformations of identical data will yield different transformed data.[1] New transformations need to be developed to simplify the comparison of high dimensional data sets. Another related problem is the automated discovery of cellular subpopulations. Many techniques have been developed to do this with varying degrees of success but the inevitable integration of multiple types of data (e.g. fluorescence and gene sequences) will necessitate more complex models that can handle the nature and variance of different classes of information.[2–4]

Another major barrier to increased degrees of multiplexing is the need for cell sorting. Commonly used data visualization transformations and population discovery algorithms are computationally intensive and require knowledge of the entire cellular population. Development of visualization and population discovery algorithms that are compatible with the low latencies required in cell sorting will be crucial to our ability to use cytometry in cellular therapies. Additionally, new approaches to cell sorting such as probabilistic modeling of cellular populations will help us break away from classical gating strategies that rely on humans to interpret data.

Overall, the field of cyometry is rapidly evolving. It is clear that future technologies will measure an ever-increasing number of cellular properties at higher and higher throughputs. The major risk in the field is that our ability to measure properties will outstrip our ability to visualize and interpret results. If these problems are avoided, however, new cytometry technologies will help break down the barriers between siloed fields of study such as genomics, cell mechanics, and biochemistry. Integrating the knowledge from each of these fields will be crucial to develop a deep understanding of how the cell functions and what occurs during disease. The future of cytometry lies in close collaboration among biologists, engineers and computer scientists.

5.1 References

[1] El Ad David Amir et al. "ViSNE enables visualization of high dimensional single-cell data and reveals phenotypic heterogeneity of leukemia". In: *Nature Biotechnology* 31.6 (May 2013), pp. 545–552. arXiv: NIHMS150003.

[2] Peng Qiu et al. "Extracting a cellular hierarchy from high-dimensional cytometry data with SPADE". In: *Nature Biotechnology* 29.10 (Oct. 2011), pp. 886–891.

[3] Nikolay Samusik et al. "Automated mapping of phenotype space with single-cell data." In: *Nature methods* 13.6 (2016), pp. 493–6.

[4] Nima Aghaeepour et al. "Critical assessment of automated flow cytometry data analysis techniques." In: *Nature methods* 10.3 (Mar. 2013), pp. 228–38.